Max-Planck-Gesellschaft
Fritz-Haber-Institut
Novel Material Discovery Group (NOMAD)

Technische Universität Berlin
- Fakultät II -
Institut für Theoretische Physik

**Masterarbeit**

# Assessing Electronic Transport in Solid Materials via the Fluctuation-Dissipation Theorem

Florian Fiebig, B. Sc.
Studiengang Master Physik
Matrikel-Nr. 337308

Berlin, 27.7.2023

Gutachter: Dr. C. Carbogno und Prof. Dr. A. Knorr

**Abstract**

For the first-principles evaluation of electronic heat and charge transport coefficients, the Kubo-Greenwood formalism represents an appealing alternative to perturbative approaches, since it naturally incorporates all orders of anharmonic and vibronic effects. In practice, however, Kubo-Greenwood calculations often come with prohibitive computational costs, since crystalline materials typically require both dense reciprocal-space **k**-grids for the electronic degrees of freedom and large real-space supercells for the vibrational ones. This is especially challenging for the charge transport coefficient of intrinsic semiconductors with dispersive electronic structures, because the free carriers are very localised in **k**-space, which demands an extremely fine **k**-grid.

In this work, we implement and investigate the application of the Fourier interpolation that can facilitate access to the extremely fine **k**-grids necessary to establish convergence. This enables the use of very dense **k**-grids for the evaluation of the Kubo-Greenwood formula, while **k**-grids used during the self-consistency cycle must only be dense enough to converge the total energy, which can typically be accomplished with substantially coarser **k**-grids.

As demonstrated for Silicon, this enables us to achieve **k**-grid convergence of the electrical conductivity spectrum with reduced computational resources. In other words, we can obtain **k**-grid convergence for systems, for which this was impossible before. This constitutes an important step towards affordable, fully anharmonic predictions of electronic heat and charge transport coefficients for all crystalline materials.

## Zusammenfassung

Zur Bestimmung der elektronischen Wärme- und Ladungstransportkoeffizienten stellt der Kubo-Greenwood-Formalismus eine reizvolle Alternative zu störungstheoretischen Methoden dar, weil er auf natürliche Weise alle Ordnungen von Anharmonizitäten berücksichtigt. Die Kubo-Greenwood-Rechenkosten sind allerdings oft so hoch, dass die Durchführung der Berechnung unmöglich ist, weil kristalline Materialien gleichzeitig ein dichtes, reziprokes Gitter zum Erfassen der elektronischen Freiheitsgrade und eine große Realraum-Superzelle für die phononischen Freiheitsgrade benötigen. Eine besondere Herausforderung stellt die elektrische Leitfähigkeit von intrinsischen Halbleitern mit dispersiven Elektronenstrukturen dar, weil die freien Ladungsträger im reziproken $\mathbf{k}$-Raum extrem lokalisiert sind, sodass ein sehr feines $\mathbf{k}$-Gitter erforderlich ist.

In dieser Arbeit implementieren und untersuchen wir die Anwendung der Fourier-Interpolation, um entsprechend feine $\mathbf{k}$-Gitter zugänglich zu machen. So wird zur Auswertung der Kubo-Greenwood-Formel ein sehr feines $\mathbf{k}$-Gitter mithilfe der Fourier-Interpolation berechnet, während in der Selbstkonsistenz-Schleife ein $\mathbf{k}$-Gitter verwendet werden kann, das lediglich dicht genug ist, um die Gesamtenergie zu konvergieren, was typischerweise mit deutlich gröberen $\mathbf{k}$-Gittern erreicht werden kann.

Wie wir für den prototypischen Halbleiter Silizium in dieser Arbeit gezeigt haben, können wir dadurch das elektrische Leitfähigkeitsspektrum in Bezug auf das $\mathbf{k}$-Gitter mit Rechenkapazitäten konvergieren, mit denen dies zuvor unmöglich war. Damit ist ein wichtiger Schritt auf dem Weg zu bezahlbaren, elektronischen Wärme- und Ladungstransportkoeffizienten gemacht, die elegant alle Ordnungen von Anharmonizitäten berücksichtigen.

# Selbstständigkeitserklärung

Hiermit erkläre ich, dass ich die vorliegende Arbeit selbstständig und eigenhändig sowie ohne unerlaubte fremde Hilfe und ausschließlich unter Verwendung der aufgeführten Quellen und Hilfsmittel angefertigt habe.

Berlin, _____

_____

[Florian Fiebig]

# Contents

# 1. Introduction

Electronic transport is ubiquitous in the modern world. It empowers everyday technologies such as washing machines, cell phones, ovens, computers, and trains. But the ability to transport electrons is very different from one material to another. Conductivity values span over many orders of magnitudes, as the following examples of electrical conductivities at room temperature show: Mullite ceramic, an insulator, has a low charge conductivity of $5.0 \times 10^{-10}$ S/cm [1]. The semiconductor silicon has an intrinsic conductivity of $3.2 \times 10^{-6}$ S/cm [2], which can be increased by orders of magnitude when foreign atoms are added as dopants. The metal copper has a very high conductivity of $5.8 \times 10^{5}$ S/cm [3].

Multiple theories for the explanation and prediction of electrical conductivity have emerged in the past century. In 1900, Paul Drude published a microscopic model of electron transport, which explained the Wiedemann-Franz law [4], but failed to explain the tremendous differences in conductivities between insulators, semiconductors and metals [5, 6]. A qualitative understanding of the involved physics was achieved by Felix Bloch, who applied the newly developed quantum mechanics to solids and explained the discrete nature of electronic energy bands in 1929 [7].

The dynamics based on the electronic band structure can be described in a semiclassical model in the framework of the Boltzmann-transport equation (BTE), which enables one to make quantitative predictions of conductivities. However, it is usually based on the harmonic approximation for nuclear interactions [8]. The influence of the harmonically approximated nuclear motion on the electronic structure is then treated in a perturbative way. These approximations may be too strong for some materials, especially when high temperature or mobile species are involved.

The Kubo-Greenwood (KG) approach constitutes an appealing alternative to BTE. It relates the conductivity, a non-equilibrium quantity, to the autocorrelation of fluctuations of the current density in equilibrium and is thus an application of the fluctuation-dissipation theorem. In particular, it naturally includes all orders of nuclei-nuclei interaction and accounts for changes in the electronic structure in response to the nuclear motion without further perturbative approximations [9, 10].

Despite its theoretical generality, the KG method is rarely used [11–15], largely because of the high computational costs. For some materials the computational costs are exorbitant and not affordable, even with modern supercomputers. The high costs stem from the required combination of large supercell sizes to map the phononic degrees of freedom and dense $\mathbf{k}$-grids to map the electronic ones accurately.

As mentioned, the $\mathbf{k}$-grid sampling required for accurate KG predictions is a crucial factor of computational costs. So far, the Kubo-Greenwood approach has only been applied to such systems, where $\mathbf{k}$-grid convergence is relatively easy to achieve. Here, we want to point out the typical easing factors:

1) In metals [12–14], a high electronic density of states (DOS) is located at the Fermi energy. At nonzero temperatures, this leads to numerous free carriers, which are spread out over a significant volume of the **k**-space. Although this still requires a dense **k**-grid, it is not as problematic as for semiconductors, for which the carriers are additionally localised.

2) In dense liquid hydrogen at high temperatures from 1000K up to 50 000K [11], the order of the system is low compared to crystalline solids. The missing translational invariance fosters localised states in direct space, which correspond to delocalised, flat states in **k**-space. As an illustration, electrons close to the nucleus are very localised in real space and show completely flat bands. For such flat bands, **k**-grid and supercell convergence is easier to achieve with the KG method.

Thermoelectric materials are an especially interesting material class for the KG approach. Many processes involve the dissipation of enormous amounts of waste heat to the environment, e.g., more waste heat is gathered in the process of extracting electrical energy from fuels than electrical energy itself (see figure A.1 in the appendix). Thermoelectric materials convert a part of this waste heat into useful electrical energy. The efficiency of this conversion benefits from low thermal and high electrical conductivity. Semiconductors can exhibit the combination of a low thermal conductivity with a simultaneous high electrical conductivity by doping. The low thermal conductivity correlates with the anharmonicity of the material (see figure A.3 in the appendix), which is naturally incorporated to all orders in the KG approach. Thus the search for more efficient thermoelectrics is an important, potential application for KG, although it is particularly challenging due to the typical, dispersive electronic structure of semiconductors.

Studies of semiconductors with the KG approach are hence very rare, because of the special challenges that this material class poses to **k**-grid convergence. In contrast to conductors, the Fermi energy for semiconductors is located between valence band maximum (VBM) and a conduction band minimum (CBM), i.e., inside the band gap. Thus there are no electronic states at the Fermi energy. Therefore the energy needed for the generation of free charge carriers by thermal excitation is much higher. Excitation and thus conduction is consequently less likely. The free charge carriers are highly localised in **k**-space in the region of the VBM and CBM. Thus an extremely fine **k**-grid is needed to map these regions appropriately. The calculation of more **k**-points is connected with higher memory and computation time costs. The larger memory costs stem from more matrices needed for the **k**-space representation of the Hamiltonian, which must be held in memory simultaneously during the self-consistent cycle. The diagonalisation of more **k**-space Hamiltonian matrices also leads to increased computation time.

The only semiconductor, which as been studied with the KG approach to our knowledge, is $Cu_{12}Sb_4S_{13}$ [15]. The KG-conductivity converges at relatively low **k**-grid densities for this particular material, because both easing factors outline before apply here: First, the translational symmetry is relatively low as implied by relatively many atoms in the primitive unit cell. Second, in contrast to typical semiconductors, the Fermi level of this material is not located in the energy gap, but at an energy with a high DOS belonging to the valence band.

In this thesis, we explore routes to access denser **k**-grids with reduced computational costs. In particular, we test if Fourier interpolation might alleviate this issue. Based on a sparse **k**-grid that is still dense enough to converge the total energy, the Fourier interpolation gives access to denser **k**-grids at reduced costs.

Focal point of this thesis is to test the Fourier interpolation as a tool in KG transport and make **k**-grid convergence feasible even for challenging materials.

To examine this, we choose a particularly challenging test system with a dispersive band diagram: silicon. Note, that for silicon the harmonic approximation of nuclei-nuclei interaction is valid. Thus the Boltzmann-transport equation can provide accurate results. Accordingly there are agreeing reference values of BTE theory and experiment, which we can compare our own results to [16].

Additionally the validity of the harmonic approximation allows to save computational time in the nuclear dynamics and incorporate the quantum behaviour of Si nuclei by drawing from the Bose-Einstein distribution.

# 2. Methods

This chapter introduces the methods and concepts used to produce the results presented in this thesis. The first section is an introduction to density-functional theory, the most common method to compute the electronic structure of solids numerically. This information is the basis for quantitative predictions of electrical conductivity. Section two informs about the Fourier approximation that allows to cut costs in the calculation of the electronic structure. The crystalline geometry can be calculated assisted by DFT, which is briefly presented in section three. Since electrical conductivity is influenced by the nuclear motions, section four discusses the harmonic approximation, which largely simplifies the calculation of these nuclear motions. Next, we turn to electronic transport theories. Starting with the Drude model as one of the first attempts to explain electrical conductivities in solids from a microscopic model. It unfortunately fails to explain the tremendous difference in electrical conductivities between material classes. For this, section six offers a qualitative explanation in terms of the Bloch model by including quantum mechanics into the microscopic picture. The seventh and eighth section show two different approaches for quantitative predictions of electrical conductivities in solids based on first principles theory, namely the Boltzmann-transport and the Kubo-Greenwood approach.

## 2.1. Density Functional Theory

Density-functional theory (DFT) takes into account the electron-electron correlation, which is essential for interatomic bonding, and makes a solution of the many-electron Schrödinger equation computationally feasible. We first illustrate the problem that DFT alleviates. After that, we present a brief introduction to the theory itself, of which the exchange-correlation functional is a vital building block. Subsequently the local density approximation is discussed as one approximation of the exact exchange-correlation functional. Finally, the mechanisms of FHI-aims, a software package for the numerical evaluation of DFT used in this work, are sketched with emphasis on its applications to crystalline materials.

### 2.1.1. The Problem

In contrast to the analytical solution of the Schrödinger equation for the hydrogen atom, there is no analytical solution of the Schrödinger equation for systems with two or more electrons. Thus we must look for numerical solutions. A common approach to solve partial differential equations (PDEs) numerically is the finite difference method (FDM). Here the function described in the PDE is evaluated on a discrete grid, such that derivatives become simple fractions. Thereby, the differential equation is converted into a system of linear equations, which can be efficiently solved by a computer. But in the case of quantum systems, these calculations become too large rapidly. In contrast to

classical particles, electrons are not localized, but waves. For the evaluation of a field, which depends on $N$ coordinates with $M$ sampling points along each coordinate, $M^N$ values must be stored. For example, an electric field with 10 grid points along each spatial direction needs $10^3 = 1000$ values of storage space. Let us look at the simple quantum example of the unit cell of silicon in the diamond structure: The primitive unit cell has a volume of $a^3/4$ with $a = 5.43$Å, which results in circa 40 000 FDM-grid points at a reasonable distance between grid points of 0.1Å. Even if we only take into account the four valence electrons of the two silicon atoms, this results, together with the two nuclei, in $40000^{10} \approx 10^{46}$ complex numbers to be stored [17]. This is infeasible even on modern supercomputers. If the $N$-electron field could be split into the superposition of one-electron fields, one would face only the manageable amount of $40000 \times 10 = 4 \times 10^5$ complex numbers. But this splitting of the system is not allowed for the exact solution of the wavefunction problem, because one would lose the correlation between particles in the wavefunction model. The neglection of the electron-electron correlation is a possible option to make the computations feasible, which is discussed in the next paragraph. In the electronic density model, however, this splitting can be done, while correlation is still taken into account, as presented in the next subsection.

For instance, the neglection of the correlation energy in the Hartree and Hartree-Fock method leads to a clear underestimation of chemical bonding in molecules and solids [18]. Nonetheless let us discuss the main idea here: Hartree's method computes the orbital of a single electron in an effective potential. First, an initial guess is made for each single-electron orbital. After that, a loop starts: From the superposition of the orbitals and positions of the nuclei an effective Coulomb potential is deduced. The Schrödinger equation for a single electron in this effective potential is then a one-body problem, which can be solved efficiently. The solution itself is an input of the effective potential in the next iteration, which closes the loop. This loop runs, until the changes in orbitals and the corresponding energies fall below a chosen threshold. This procedure leads to a self-consistent field (SCF) of wavefunctions. Hartree's method works fine to bind electrons into atoms. It can be extended to the Hartree-Fock procedure, which additionally takes into account the exchange energy, that stems from antisymmetrizing the ansatz for the wavefunction due to the indistinguishability of the electrons [19]. Nevertheless, the Hartree- and Hartree-Fock method underestimate the bonding energies and overestimates bond lengths, because of their neglection of the correlation energy. The SCF procedure, however, is also employed in DFT.

### 2.1.2. Density-Functional Theory

Density-functional theory (DFT) is a reformulation of the wavefunction problem that provides the opportunity to reasonably approximate the exchange-correlation energy at feasible costs. Here, we first discuss DFT in general, before turning to the local density approximation, the most basic exchange-correlation approximation.

We can alleviate the computational problem discussed above, if we can switch from the electronic wavefunction with $3N$ coordinates as the central variable of our problem to the electronic density with only 3 coordiantes. To transform the wavefunction problem into an electronic-density problem, we first connect the total energy of the wavefunction problem to energy of the electron-density problem. For the true ground state, both energies must be equal. The total energy of the ground state of an electron gas depends only on the electron density, which was shown in 1964 by Hohenberg

and Kohn with a proof by reductio ad absurdum [20]. Furthermore the total energy of the electron gas can be split into two parts: One depending on the electronic density $n(\mathbf{r})$ and the external potential $v_{ext}(\mathbf{r})$ and the other being a functional $F$ of the electron density alone:

$$E = \int n(\mathbf{r}) v_{ext}(\mathbf{r}) d\mathbf{r} + F[n(\mathbf{r})]. \tag{2.1}$$

The exact form of the later functional $F$ remains unknown until today. Possibly, there exists no exact analytical form for the functional at all.

With $F[n(\mathbf{r})]$ unknown, the equation above cannot be used to find the energy or the electronic density of the system. Kohn and Sham were shedding light on the dependence of the energy on the electronic density in 1965 [21] by reintroducing artificial single-particle wavefunctions. While this looks like reintroducing the problems illustrated before at first glance, it is not for two reasons: First, the single particles are modelled to be independent of each other moving in an effective potential, which overcomes the computational problem mentioned before. Second, in the effective potential the correlation of the electrons can be included, which alleviates the accuracy issue. The effective potential is constructed such that the ground state of the non-interacting electrons and the ground state of the interacting electrons are equal. The non-interacting electrons have the kinetic energy of independent electrons and a potential energy that includes the mean-field Coulomb repulsion (Hartree term) and the exchange-correlation functional $E_{xc}$, which corrects for the neglected interaction effects.

We seek the electronic density associated with the smallest total energy. The minimization is constrained by a fixed number of electrons. This is mathematically enforced via Lagrange multipliers, here named $\epsilon_i$. After executing variational calculus, one obtains the following single-particle equation:

$$\underbrace{\left( \frac{-\hbar^2}{2m}\nabla^2 + v_{ext}(\mathbf{r}) + \frac{e^2}{4\pi\epsilon_0} \int n(\mathbf{r}) \frac{1}{|r - r'|} d\mathbf{r}' + \frac{\delta}{\delta n} E_{xc}[n(\mathbf{r})] \right)}_{h^{KS}} \Psi_i(\mathbf{r}) = \epsilon_i \Psi_i(\mathbf{r}) \,, \tag{2.2}$$

with $m$ the mass of an electron, $\hbar$ Planck's reduced constant, $\epsilon_0$ the electric constant, $e$ the elementary charge, and $h^{KS}$ the Kohn-Sham Hamiltonian. Self-interaction is included, because a sum over all electrons (including the i-th electron) enters the Coulomb potential in the Schrödinger equation for the i-th electron.

The electronic density is then recovered as the superposition of the probability density of the artificial single-electron wavefunctions $\Psi_i(\mathbf{r})$:

$$n(\mathbf{r}) = \sum_{i=1}^{N} |\Psi_i(\mathbf{r})|^2 \,. \tag{2.3}$$

The electronic density depends on the single-particle wavefunction, because the first is the sum of the squared modulus of the later. In turn, the single-particle wavefunction depends on the electronic density, because the potential of this density is part of the single-particle Schrödinger equation,

which determines the single-particle wavefunction. Thus the two equations above can only be solved self-consistently. Once the change of the total energy of the system falls below a certain threshold, the self-consistency loop stops, yielding a result for the single-particle wavefunctions and the density.

With this framework, one can now, in principle, acquire the exact energy and electronic density. The analytic form of the exchange-correlation energy $E_{xc}[n(\mathbf{r})]$, however, is unknown and thus approximations for it must be made in practise.

### 2.1.3. Local Density Approximation (LDA)

For the unknown $E_{xc}[n(\mathbf{r})]$ different approximations have been developed over the years. The first instance is the local density approximation, which was published directly with the self-consistent single-particle equations above [21]. It transfers knowledge from jellium, an idealized system of electrons with a uniform electronic density on a homogeneously and positively charged background, to systems with non-uniform electronic densities. Analytic expressions for the exchange-correlation energy of jellium in the high- and low-density limit exist [22, 23] and intermediate values can be computed with quantum Monte-Carlo [24]. For a slowly varying electronic density, one can assume that the exchange-correlation part is the integral of the electronic density multiplied with the exchange-correlation functional of the homogeneous electron gas $\epsilon_{xc\ hom}(n)$ [21], which was assumed to be known [25]:

$$E_{xc}[n(\mathbf{r})] = \int d\mathbf{r}\ n(\mathbf{r})\epsilon_{xc\ hom}(n(\mathbf{r}))\ . \tag{2.4}$$

### 2.1.4. FHI-aims

To solve DFT's self-consistent set of equations, one typically expands the solutions $\Psi_l$ into a linear combination of basis functions $\varphi_l$ with coefficients $c_{il}$ such that $\Psi_l = \sum_{i=1}^{N_{\text{basis}}} c_{il}\varphi_l$. One can choose between different sets of basis functions, such as plane waves [26, 27] or numerical atom-centered orbitals (NAOs) [28]. A larger number of basis functions $N_{\text{basis}}$ leads to more accurate solutions, but also to higher computational costs. In the FHI-aims [28], element-specific NAOs of the form

$$\varphi_i(\mathbf{r}) = Y_{lm}(\Omega)\frac{1}{r}u_i(r) \tag{2.5}$$

are chosen as the basis set, where $u_i(r)$ describes the orbital's radial shape with $r$ the magnitude of the position vector $\mathbf{r}$ and $Y_{lm}(\Omega)$ is a spherical harmonic. This transfers the problem into an algebraic, generalized eigenvalue problem of finding the coefficients of the basis functions:

$$\sum_j h_{ij}c_{jl} = \epsilon_l \sum_j s_{ij}c_{jl}\ , \tag{2.6}$$

where $s_{ij} = \int d^3r\varphi_i(\mathbf{r})\varphi_j(\mathbf{r})$ are the matrix elements of the overlap matrix and $h_{ij} = \int d^3r\varphi_i(\mathbf{r})h^{KS}\varphi_j(\mathbf{r})$ the matrix elements of the Kohn-Sham Hamiltonian $h^{KS}$ in equation (2.2).

The function $u_i(r)$ is strictly localised with values of zero outside of a cutoff radius. For this reason, the matrices in equation (2.6) are sparse, which makes systems with thousands of atoms routinely computable on modern computational resources.

However in macroscopic crystals, the number of atoms is in the order of magnitude of $10^{23}$, which is clearly not computable. One challenge is to calculate wavefunctions for so many electrons. The second challenge is that also these wavefunctions span over a very large region spatially. Both challenges can be overcome by introducing periodic boundary conditions at the borders of spatially limited supercells [29] and applying Bloch's theorem [26]. According to Bloch's theorem [7] electronic states in periodic potentials have the form $\Psi_{\mathbf{k}}(\mathbf{r}) = \exp(i\mathbf{kr})\, u(\mathbf{r})$ , where $\mathbf{k}$ is a reciprocal lattice vector and $u(\mathbf{r})$ is a function of the same periodicity as the real-space lattice (more details in section 2.6).

After introducing periodic boundary conditions, the Bloch waves feature $\mathbf{k}$-phases, which are compatible with the applied periodic boundary conditions. The density of the compatible $\mathbf{k}$-points is proportional to the volume, which is enclosed by the boundary conditions. The infinite number of electrons in the infinite crystal corresponds to an infinite number of $\mathbf{k}$-points, for each of which only a finite number of wavefunctions are occupied. The calculation of infinitely many electronic wavefunctions has thus been transfered to computing a limited number of wavefunctions at infinitely many $\mathbf{k}$-points. But the electronic waves at different $\mathbf{k}$-points converge to each other as the distance between the $\mathbf{k}$-points becomes smaller and smaller. We can thus represent the wavefunctions over a $\mathbf{k}$-space neighbourhood by the wavefunctions at a single $\mathbf{k}$-point. Therefore only a finite number of $\mathbf{k}$-points with corresponding wavefunctions are needed for the accurate description of the electronic structure of crystals. [26]

In the case of periodic boundary conditions, the basis functions in FHI-aims [28] take the form

$$\chi_{i,\mathbf{k}} = \sum_{\mathbf{N}} \exp(i\mathbf{k}\mathbf{T}(\mathbf{N}))\varphi_i(\mathbf{r} - \mathbf{R}_{\text{atom}} + \mathbf{T}(\mathbf{N})) \,, \tag{2.7}$$

where $\mathbf{R}_{\text{atom}}$ is the position of an atom relative to the containing cell, $\mathbf{T}(\mathbf{N})$ is the translation operator by $\mathbf{N} = (N_x, N_y, N_z)$ cells in each spatial direction, which are possible inside the periodic boundary conditions. These basis functions automatically fulfil Bloch's theorem. They also lead to $\mathbf{k}$-dependent Hamiltonian and overlap matrices and, of course, $\mathbf{k}$-dependent solutions for the electronic wavefunctions.

The matrix elements of the Hamiltonian are also $\mathbf{k}$-dependent

$$h_{ij}(\mathbf{k}) = \langle \chi_{i,\mathbf{k}} | h^{KS} | \chi_{j,\mathbf{k}} \rangle = \sum_{\mathbf{N},\mathbf{M}} \exp(i\mathbf{k}(\mathbf{T}(\mathbf{N}) - \mathbf{T}(\mathbf{M})))\langle \varphi_{i,\mathbf{N}} | h^{KS} | \varphi_{j,\mathbf{M}} \rangle \,, \tag{2.8}$$

Since the summands only depend on the difference between $\mathbf{N}$ and $\mathbf{M}$, we can fix $\mathbf{N} = (0, 0, 0)$ and let only $\mathbf{M}$ take on different values:

$$h_{ij}(\mathbf{k}) = \sum_{\mathbf{M}} \exp(-i\mathbf{k}\mathbf{T}(\mathbf{M}))\langle \varphi_{i,0} | h^{KS} | \varphi_{j,\mathbf{M}} \rangle \,, \tag{2.9}$$

which is in principle an infinite sum for an infinite supercell. In the next section, we will see that this infinite sum can be truncated after including sufficiently many unit cells.

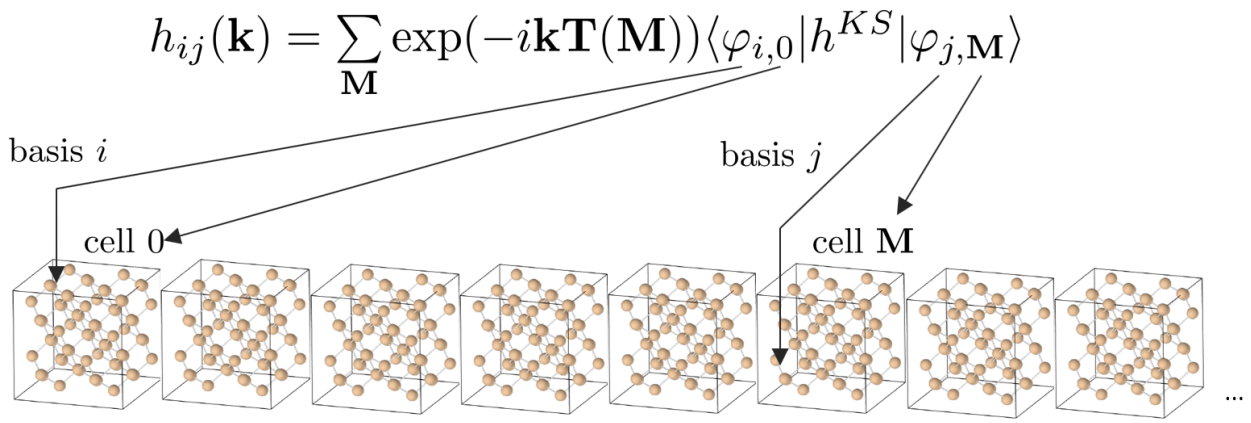


**Figure 2.1.:** Exemplary identification of the elements of the **k**-dependent Hamiltonian with real-space cells along one axis, which are here shown to be not touching each other in contrast to reality for clarity's sake.

## 2.2. Fourier Interpolation

We can exploit the fact that the Fourier series in equation (2.9) can be truncated to generate **k**-points at lower computational costs from a **k**-point converged Hamiltonian by applying the Fourier interpolation (see figure 2.2).

The overlap between two basis functions from different cells becomes smaller and smaller, when the distance between the cells grows, i.e., $h_{0i,\mathbf{M}j} \to 0$ when **M** or respectively the supercell size $L \to \infty$. The sum over **M** can thus be truncated, once the basis function overlap is vanishing (see figure 2.2).

Writing out the sum, for example for 8 cells, we obtain the formula shown in figure 2.2. Since the overlap between basis functions becomes weaker and weaker with growing distance, the last parts of the sum become smaller and smaller and finally become exactly zero due to the strictly localised NAOs in FHI-aims.

For silicon, for instance, the **k**-grid convergence of the total energy is already achieved at a 4x4x4 **k**-grid in a 64-atom supercell, since the corresponding supercell has become so large that the overlap between basis functions from different unit cells starts vanishing at this point (see figure 2.2). For the KG-conductivity spectrum, such a 4x4x4 **k**-grid is clearly underconverged, as discussed in subsection 3.4.1.

Denser **k**-grids are equivalent to larger supercells. For larger supercells respectively denser **k**-grids, the matrices become sparse. The number of matrices, however, is still growing linearly with number of **k**-points requested.

The maximum memory per node has been growing linearly with the number of **k**-points and was already significant at a 16x16x16 **k**-grid (see subsection 3.4.1), because a Hamiltonian matrix $h_{ij}(\mathbf{k})$, an overlap matrix $s_{ij}(\mathbf{k})$ and a solution $\Psi(\mathbf{k})$ for each **k**-point are held in the memory during the SCF cycle. To reduce the memory consumption, we must reduce either the size of the matrix $h_{ij}(\mathbf{k})$ or the number of matrices, i.e., the number of **k**-points.

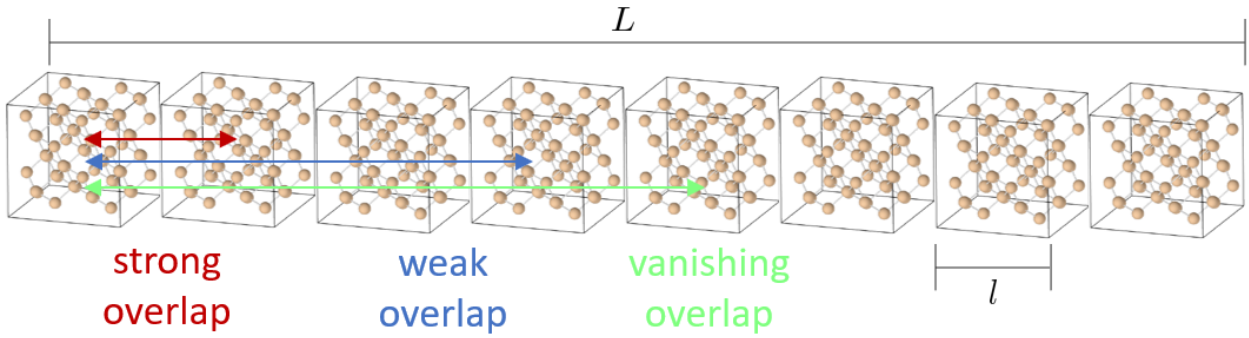


$$h_{ij}(k) = \sum_M \exp(-i2\pi \tfrac{l}{L} Mk) h_{0i,Mj} = \begin{aligned} &\exp(-i2\pi \tfrac{l}{L} 0k) h_{0i,0j} \\ &+ \exp(-i2\pi \tfrac{l}{L} 1k) h_{0i,1j} \\ &+ \exp(-i2\pi \tfrac{l}{L} 2k) h_{0i,2j} \\ &+ \exp(-i2\pi \tfrac{l}{L} 3k) h_{0i,3j} \\ &+ \exp(-i2\pi \tfrac{l}{L} 4k) h_{0i,4j} \\ &+ \exp(-i2\pi \tfrac{l}{L} 5k) h_{0i,5j} \\ &+ \exp(-i2\pi \tfrac{l}{L} 6k) h_{0i,6j} \\ &+ \exp(-i2\pi \tfrac{l}{L} 7k) h_{0i,7j} \end{aligned} \Big\} \approx 0$$

**Figure 2.2.:** Qualitative visualisation of overlap weakening with growing distance and its meaning for the summands of the **k**-dependent Hamiltonian. The visualisation matches the **k**-grid convergence of the total energy for the 64-atom supercell of Si.

Once we provided enough **k**-points for total energy and electron density to be converged in the SCF cycle, we can use the converged Hamiltonian to compute the electronic structure for further **k**-points without the SCF cycle. If we were to compute them during the SCF cycle, all requested **k**-points would to be stored in memory simultaneously, which soon becomes infeasible for the dense **k**-grids needed to converge the electrical conductivity spectrum of semiconductors with KG. Using the Fourier interpolation, we can calculate further **k**-points one by one after the SCF cycle on the basis of the SCF **k**-grid, which greatly reduces the memory needed for dense **k**-grids.

However, this approximation is only justified, if all summands in the formula in figure 2.2 with relevant contributions are kept. For too small SCF **k**-grids, Fourier interpolation leads to artefacts, but it quickly becomes stable, typically already for those relatively sparse **k**-grids needed to converge the total energy. The size of the SCF **k**-grid needed for convergence differs from material to material, but can easily be determined with a study of convergence.

The application of the Fourier interpolation will enable us to **k**-point converge the KG electrical conductivity spectrum of the 64-atoms supercell as demonstrated in subsection 3.4.2.

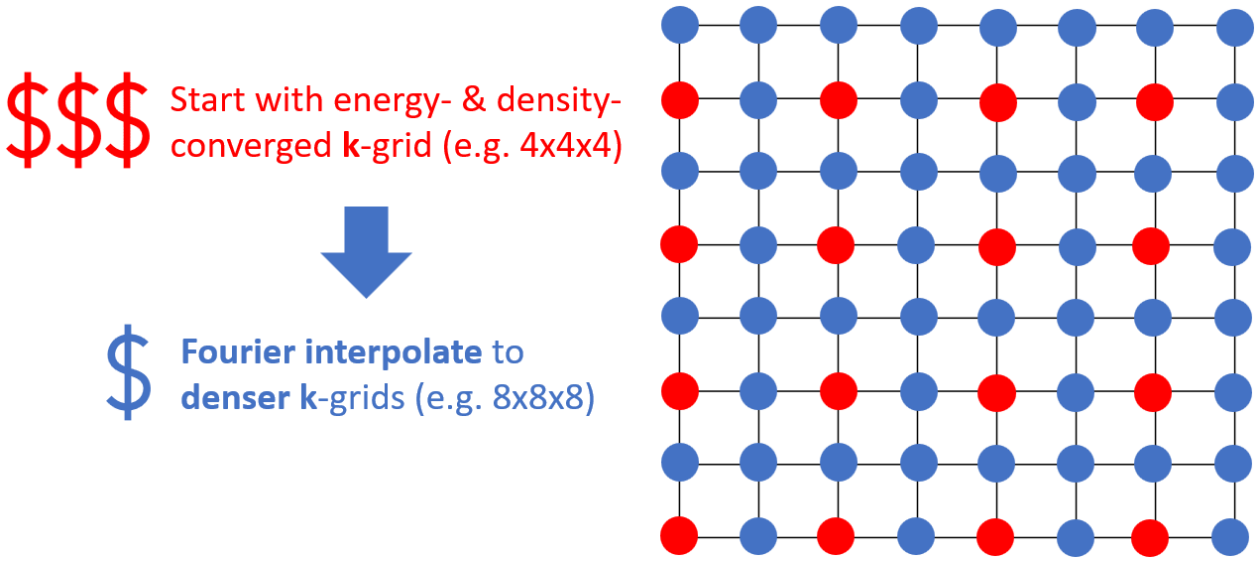


**Figure 2.3.:** Schematic 2D visualisation of the 4x4x4 self-consistent field **k**-grid, which is then extended to a 8x8x8 **k**-grid by Fourier interpolation.

## 2.3. Geometry Relaxation

Often one is interested in the atomic geometry of a crystal. This can be found by looping over individual DFT calculations: Given the initial guess of the position of the nuclei, the electronic structure and the total energy are computed. Next, the force on a nucleus can be evaluated as the negative gradient of the total energy with respect to the position of a nucleus. After that, the nucleus is moved in the direction of the force for a distance, which is proportional to the magnitude of the force (Euler step). Once the positions of all nuclei are updated in this fashion, the electronic structure and total energy are calculated anew and the loop restarts. Once these forces are small enough, a relaxed structured is found, which we can see in figure 2.4 for a supercell with 64 Si atoms. The relaxation was performed with FHI-aims [28]. The Hellmann-Feynman theorem saves us a numerical evaluation of the derivative of the wavefunction $\Psi_{\mathbf{r}_i}$ with respect to the nucleus's position $\mathbf{r}_i$ and enables us to execute the derivative on the Hamiltonian $H_{\mathbf{r}_i}$ only [30, 31]: $\nabla_{\mathbf{r}_i} E_{\mathbf{r}_i} = \langle \Psi_{\mathbf{r}_i} | \nabla_{\mathbf{r}_i} H_{\mathbf{r}_i} | \Psi_{\mathbf{r}_i} \rangle$ .

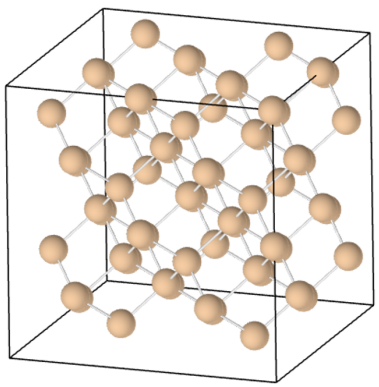

**Figure 2.4.:** Relaxed geometry of a supercell of 64 Si atoms in the diamond crystal structure calculated with DFT as implemented in FHI-aims.

## 2.4. Harmonic Approximation and Phonons

Atoms are bound to each other in a crystal. If one atom is displaced, other atoms will experience a force, too. How is one atom $j$ in unit cell $l$ influenced by the displacements $u_{j'l'}$ of the other atoms $j'$ in other unit cells $l'$?

The total energy $E_{\text{total}}$ of the system can be expanded into a Taylor series with respect to the component $\alpha \in \{x, y, z\}$ for the Cartesian directions of the displacements $u_{jl}$ of the atoms from their equilibrium positions:

$$\begin{aligned} E_{\text{total}}(u^x_{00}, ..., u^z_{nL}) = & \underbrace{E_{\text{total}}(0, .., 0)}_{\text{const} \to \frac{\partial}{\partial u^\alpha_{jl}} E_{\text{total}}(0,..,0)=0} + \sum_{\alpha,j,l} \underbrace{\frac{\partial E_{\text{total}}(0, .., 0)}{\partial u^\alpha_{jl}}}_{=0,\text{ loc. min.}} u^\alpha_{jl} + \frac{1}{2} \sum_{\alpha\beta,jj',ll'} \frac{\partial^2 E_{\text{total}}(0, .., 0)}{\partial u^\alpha_{jl} \partial u^\beta_{j'l'}} u^\alpha_{jl} u^\beta_{j'l'} + \\ & \underbrace{+ \frac{1}{3!} \sum_{\alpha\beta\gamma,jj'j'',ll'l''} \frac{\partial^3 E_{\text{total}}(0, .., 0)}{\partial u^\alpha_{jl} \partial u^\beta_{j'l'} \partial u^\gamma_{j''l''}} u^\alpha_{jl} u^\beta_{j'l'} u^\gamma_{j''l''} + \dots}_{\text{neglected in harmonic approximation}} , \end{aligned} \tag{2.10}$$

where $L$ is the total number of primitive unit cells, $n$ is the total number of atoms per primitive unit cell and we follow the presentation of the theory by Dove [32].

In the harmonic approximation, the equation of motion with the effective force on atom $j$ as the negative gradient of the total energy with respect to $\mathbf{u_{jl}}$ is:

$$m_j \frac{d^2}{dt^2} u^\alpha_{jl}(t) = -\frac{1}{2} \sum_{\beta,j',l'} \underbrace{\frac{\partial^2 E_{\text{total}}(0, .., 0)}{\partial u^\alpha_{jl} \partial u^\beta_{j'l'}}}_{\text{const}} u^\beta_{j'l'}(t) , \tag{2.11}$$

where $m_j$ is the mass of atom $j$ and $t$ is the time.

These equations of motion for the displacements can be solved analytically by a superposition of traveling waves:

$$u^\alpha_{jl}(t) = \sum_{\mathbf{q},\nu} U^\alpha_{j\mathbf{q}\nu} \exp(i(\mathbf{q}\mathbf{r}_{jl} - \Omega_{\mathbf{q},\nu} t)) , \tag{2.12}$$

where $\mathbf{q}$ is a wavevector from reciprocal space, $\mathbf{r}_{jl}$ the equilibrium position of the atom $j$ in unit cell $l$, $\Omega_{\mathbf{q},\nu}$ the temporal frequency of the lattice oscillation [1], and $\mathbf{U}_{j\mathbf{q}\nu}$ is the amplitude vector independent of $l$, since the phase difference between the unit cells is described by the phase factor. The occupation number determines the amplitude for each mode up to a phase factor, which is given by the initial conditions.

1 $\Omega_{\mathbf{q},\nu}$ is the temporal frequency of the lattice oscillation to avoid confusion with the previously mentioned temporal frequency $\omega$ of a photon.

Inserting the ansatz for $u_{jl}(t)$ into the equation of motion, one obtains a time-independent set of equations, which take the form of an eigenvalue problem:

$$D(\mathbf{q})\mathbf{e}_{\mathbf{q}\nu} = \Omega^2_{\mathbf{q}\nu}\mathbf{e}_{\mathbf{q}\nu} \ , \tag{2.13}$$

where $\mathbf{e}_{\mathbf{q}\nu}$ is a vector containing the system's re-scaled amplitude vectors

$$\mathbf{e}_{\mathbf{q}\nu} = \begin{bmatrix} \sqrt{m_1}\, U^x_{1\mathbf{q}\nu} \\ \sqrt{m_1}\, U^y_{1\mathbf{q}\nu} \\ \sqrt{m_1}\, U^z_{1\mathbf{q}\nu} \\ \sqrt{m_2}\, U^x_{2\mathbf{q}\nu} \\ . \\ . \\ . \\ \sqrt{m_N} U^z_{N\mathbf{q}\nu} \end{bmatrix} \tag{2.14}$$

and $D(\mathbf{q})$ is the so called dynamical matrix, which can be decomposed into $N \times N$ blocks with $N$ the total number of atoms in the supercell and each block describing the interaction between an atom $j$ and $j'$ and each block being a $3 \times 3$ matrix with components $\alpha\beta$:

$$D^{\alpha\beta}_{jj'}(\mathbf{q}) = \frac{1}{\sqrt{m_j m_{j'}}} \sum_{l'} \frac{\partial^2 E_{\text{total}}(0,..,0)}{\partial u^\alpha_{j0} \partial u^\beta_{j'l'}} \exp(i\mathbf{q}(\mathbf{r}_{j'l'} - \mathbf{r}_{j0})) \ . \tag{2.15}$$

The eigenvalues and eigenvectors can be computed for each $\mathbf{q}$. The relation between the square roots of the eigenvalues $\Omega^2_{\mathbf{q}\nu}$ and $\mathbf{q}$ is called dispersion relation. It characterises the relation between the spatial and temporal oscillation of the each mode $\nu$.

In complete analogy to the electronic band diagram discussed in section 2.6, the values of $\mathbf{q}$ can be confined to the first Brillouin zone and the discrete Fourier series incorporated in 2.15 can be truncated, once the distance of primitive unit cells is so large that the interaction between their atoms vanishes.

For silicon, the dispersion relation is shown in figure 2.5. To calculate the dispersion relation, we ran phonopy [33] via FHI-vibes [34]. We can see six bands in figure 2.5, one band for each spatial direction of every atom in the primitive unit cell. Three of these modes are acoustic modes displaying a zero frequency at the Γ-point labeled G. The other three modes are so called optical modes. The energy of the oscillations is quantised, i.e., it is allowed to vary only in integer steps of $\hbar\Omega$. They are called phonons as the elementary oscillations of sound waves, in analogy to photons referring to the elementary oscillations of electromagnetic waves.

Of course, modelling the bonds as springs is a severe simplification. In reality, it is the complex interplay of correlated electrons, which binds the atoms together. However, this model works

surprisingly well, for example to deduce the temperature dependence of the specific heat [35]. Phonons are also used in the Boltzmann-transport equation to model the nuclear motion. In this work, we use the analytical solutions facilitated by the harmonic approximation for the generation of harmonic samples, which is discussed in section 3.1.

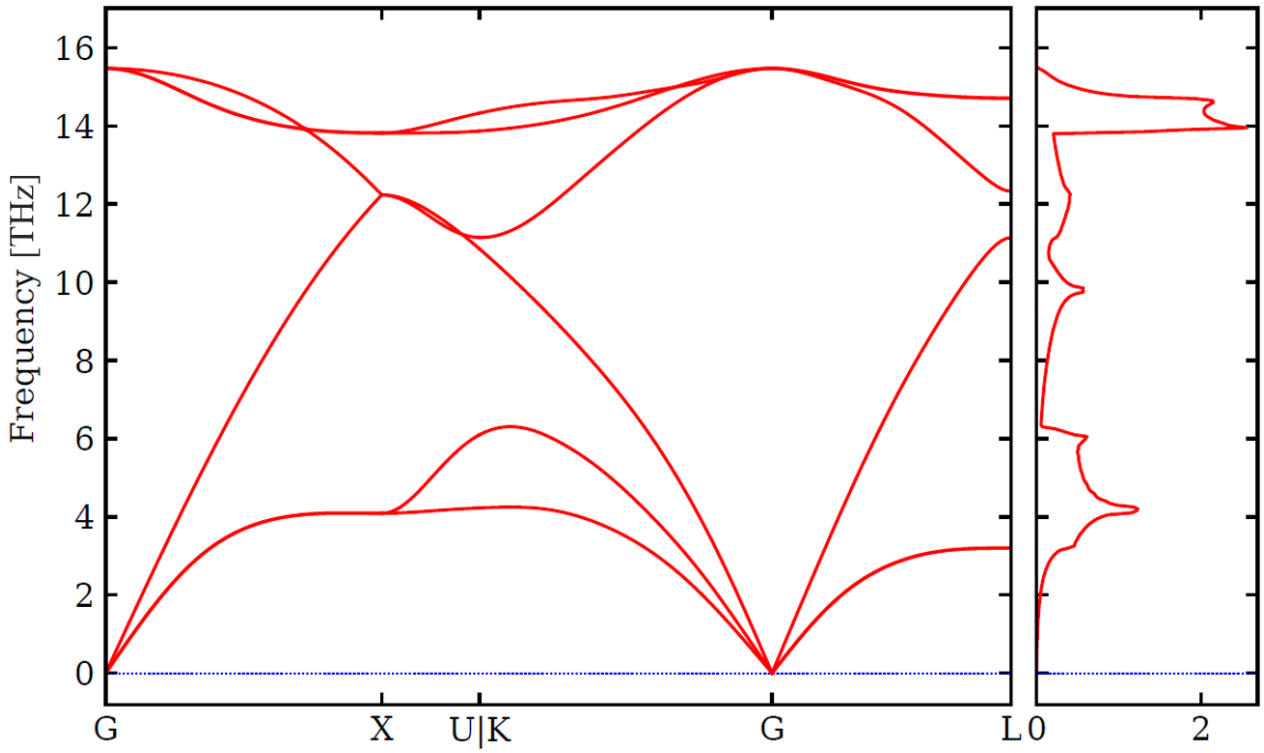


**Figure 2.5.:** Phonon-band diagram and density of states of silicon. A cubic cell with 64 Si atoms was used in the calculation.

## 2.5. Drude Model

In 1900, Paul Drude explained the phenomenon of electrical resistance in materials by the interplay of two opposing effects: the acceleration of electrons by the applied electric field and the randomization of the direction of the velocity of electrons by collisions with nuclei [5, 6] (see figure 2.6). It is assumed that the randomized velocities have a vanishing mean. Thus the collision can be seen as a deceleration of the electrons to zero velocity on average. In such a (semi-)classical model [36], the current density is:

$$\mathbf{j} = -en\mathbf{v} \,, \tag{2.16}$$

where $e$ is the elementary charge, $n$ the density of free electrons, and $\mathbf{v}$ is the average velocity of the electrons.

While electrons are assumed not to contribute to the average current right after a collision with a nucleus, they are accelerated in the opposite direction of the external electrical field in the time between collisions. This is described by the equation of motion:

$$\frac{d}{dt}\mathbf{p}(t) = -e\mathbf{E} - \frac{\mathbf{p}(t)}{\tau} \,, \tag{2.17}$$

where $t$ is the time, $\mathbf{p}(t)$ is the average momentum over all electrons, and $\tau$ is the "lifetime", i.e., the average time of unhindered acceleration between collisions. On average, this leads to a net velocity $\mathbf{v} = \frac{\tau e\mathbf{E}}{m}$ over all electrons. The current density thus becomes:

$$\mathbf{j} = \underbrace{\frac{ne^2\tau}{m}}_{=\sigma_0} \mathbf{E} \,, \tag{2.18}$$

which yields a definition of the direct-current electrical conductivity $\sigma_0$.

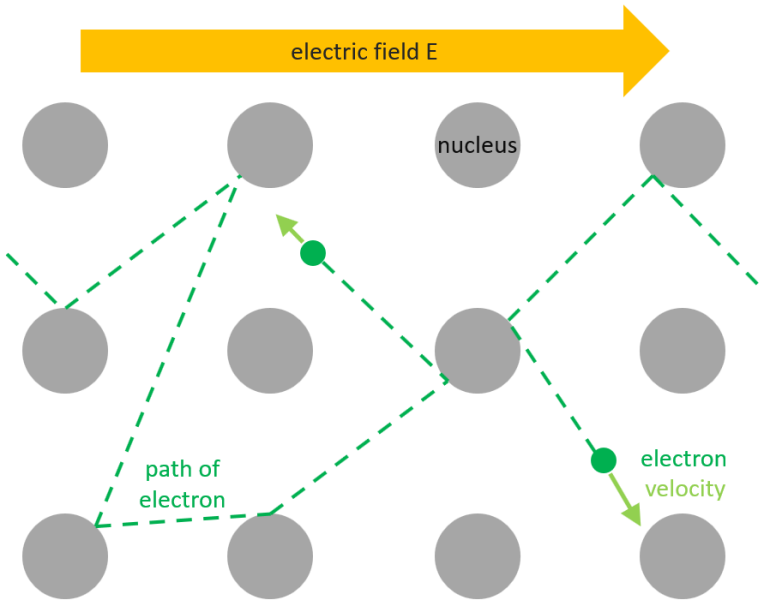


**Figure 2.6.:** Schematic visualization of Drude's model. The free valence electrons (green) are scattered by the ions (grey) in random directions after each collision. The electric field (yellow) causes an acceleration of the electrons in its opposite direction between scattering events. This results in a non-zero average velocity of the electrons in the opposite direction of the electric field.

This model suggests that electrons will collide sooner with nuclei, if a material has more nuclei per unit volume. Thus materials with more nuclei per unit volume should show lower electrical conductivity. This shows correct trends for metals, but it can easily be falsified with e.g. copper and silicon. Copper has $\approx 0.14$ mol nuclei per cm$^3$; silicon $\approx 0.08$ mol nuclei per cm$^3$. Thus copper has almost two times more hindering nuclei per unit volume than silicon, but its electrical conductivity is more than eleven orders or magnitude higher [2, 3, 37]. Therefore the Drude model cannot explain the different conductivities of conducting and isolating materials. However, its success was to explain the proportional relation between the ratio of thermal and electrical conductivity in metals and their temperature qualitatively (Wiedemann-Franz law [4]), since the same model of motion can be used for electronic heat transport with electrons as the carriers of heat instead of charge.

In case of an alternating current, the electrical field can be described in the form $\mathbf{E}(t) = \mathrm{Re}(\mathbf{E}(\omega)\exp(-i\omega t))$, with the angular frequency $\omega$. Accordingly, the average impulse $\mathbf{p}(t)$ and average current density $\mathbf{j}(t)$ take the same mathematical form. Plugging these Ansätze into Drude's equation of motion (2.17), executing the derivatives and canceling the common phase factor $\exp(-i\omega t)$), one obtains the following frequency-dependent conductivity:

$$\sigma(\omega) = \frac{\sigma_0}{1 - i\omega\tau} = \underbrace{\frac{\sigma_0}{1+\omega^2\tau^2}}_{\mathrm{Re}} + i\,\underbrace{\omega\tau\frac{\sigma_0}{1+\omega^2\tau^2}}_{\mathrm{Im}}\,, \tag{2.19}$$

with $\sigma_0 = \frac{ne^2\tau}{m}$. This relation $\sigma(\omega)$ is often referred to as Drude function.

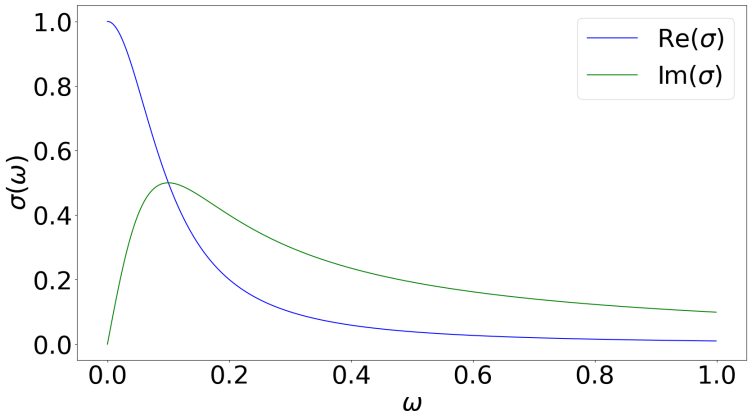


**Figure 2.7.:** Real and imaginary part of the alternating-current conductivity $\sigma(\omega)$ in arbitrary units to show the qualitative shape of the resulting curves. The real part (blue) is the inverse of the resistance and decreases monotonously from its maximum at zero angular frequency. The imaginary part (green) is the inverse of the reactance and is associated with a phase shift between the electrical field and the resulting current.

## 2.6. Bloch Model

Modelling a macroscopic crystal, Bloch describes electrons as waves according to the Schrödinger equation [38] in an infinite, periodic potential. From this periodicity, a statement about the general form of solutions of the Schrödinger equation containing this periodic potential can be deduced, for which we follow the presentation in [36]:

Due to the periodicity, the Hamiltonian $H$ is invariant with translations of primitive lattice vectors $\mathbf{R}$:

$$H(\mathbf{r}) = H(\mathbf{r} + \mathbf{R})\,. \tag{2.20}$$

The formalisation with the translation operator acting on any spatial function $f$ is:

$$T_{\mathbf{R}} f(\mathbf{r}) = f(\mathbf{r} + \mathbf{R}) \,. \tag{2.21}$$

For the concatenation of the translation operator naturally holds

$$T_{\mathbf{R}} T_{\mathbf{R}'} \Psi(\mathbf{r}) = T_{\mathbf{R}'} T_{\mathbf{R}} \Psi(\mathbf{r}) = \Psi(\mathbf{r} + \mathbf{R} + \mathbf{R}') = T_{\mathbf{R}+\mathbf{R}'} \Psi(\mathbf{r}) \,. \tag{2.22}$$

The translation operator and the periodic Hamiltonian commute:

$$T_{\mathbf{R}}(H(\mathbf{r})\Psi(\mathbf{r})) = H(\mathbf{r} + \mathbf{R})\Psi(\mathbf{r} + \mathbf{R}) = H(\mathbf{r})\Psi(\mathbf{r} + \mathbf{R}) = H(\mathbf{r}) T_{\mathbf{R}} \Psi(\mathbf{r}) \,. \tag{2.23}$$

Therefore H and $T_{\mathbf{R}}$ have the same eigenstates $\Psi(\mathbf{r})$. But applying the operators on the common eigenstates can give different eigenvalues $\epsilon$ and $C_{\mathbf{R}}$:

$$H(\mathbf{r})\Psi(\mathbf{r}) = \epsilon \Psi(\mathbf{r}) \,, \tag{2.24}$$

$$T_{\mathbf{R}} \Psi(\mathbf{r}) = C_{\mathbf{R}} \Psi(\mathbf{r}) \,. \tag{2.25}$$

Parting the lattice vector $\mathbf{R}$ into integer multiples $n_i$ of the primitive lattice vectors $\mathbf{a}_i$ and considering the concatenation property of the translation operator, we find:

$$C_{\mathbf{R}} = (C_{\mathbf{a}_1})^{n_1} (C_{\mathbf{a}_2})^{n_2} (C_{\mathbf{a}_3})^{n_3} \,. \tag{2.26}$$

$C_{\mathbf{a}_i}$ is regarded as a complex number, which can be represented as $\exp(2\pi i z_i)$ with $z_i$ another complex number. With this complex exponential representation, equation (2.27) can be rewritten more compactly as

$$C_{\mathbf{R}} = \exp(i\mathbf{k}\mathbf{R}) \tag{2.27}$$

with $\mathbf{k} = z_1\mathbf{b}_1 + z_2\mathbf{b}_2 + z_3\mathbf{b}_3$ with $\mathbf{b}_i$ reciprocal lattice vectors fulfilling $\mathbf{b}_i \cdot \mathbf{a}_j = 2\pi\delta_{ij}$. By introducing appropriate boundary conditions one can show that $z_i$ must indeed be real numbers.

Applying the translation operator on the eigenstates $\Psi(\mathbf{r})$ of H (and $T_R$) and rewriting the translational eigenvalue into the exponential form, one finds with respect to the eigenvalue

$$T_{\mathbf{R}} \Psi(\mathbf{r}) = C_{\mathbf{R}} \Psi(\mathbf{r}) = \exp(i\mathbf{k}\mathbf{R})\Psi(\mathbf{r}) \tag{2.28}$$

and

$$T_{\mathbf{R}} \Psi(\mathbf{r}) = \Psi(\mathbf{r} + \mathbf{R}) \tag{2.29}$$

with respect to the translational symmetry. In combination this yields:

$$\Psi(\mathbf{r}+\mathbf{R}) = \exp(i\mathbf{k}\mathbf{R})\Psi(\mathbf{r}) \,, \tag{2.30}$$

which is known as Bloch's theorem.

The eigenfunction of $T_\mathrm{R}$ are plane waves. All solutions of the Schrödinger equation in crystals thus share the same general form: a plane wave multiplied by a function with the same periodicity as the lattice of nuclei (figure 2.8). The full Bloch solution is hence the lattice-periodic function $u(\mathbf{r})$, which can also depend on other quantum numbers, multiplied by a plane wave $\exp(i\mathbf{k}\mathbf{r})$ (lower half of figure 2.8):

$$\Psi(\mathbf{r}) = \exp(i\mathbf{k}\mathbf{r})\, u(\mathbf{r}) \,, \tag{2.31}$$

where $\mathbf{r}$ is the position vector in Cartesian coordinates, $i$ is the imaginary unit, $\mathbf{k}$ is a continuous, real vector, which is called the crystal momentum as it shares properties with the classical impulse, but it cannot be identified completely with the impulse of the electron, because it is not the eigenvalue of the momentum operator applied to a Bloch function [36]. It can be seen as an extension of the impulse in periodic potentials though.

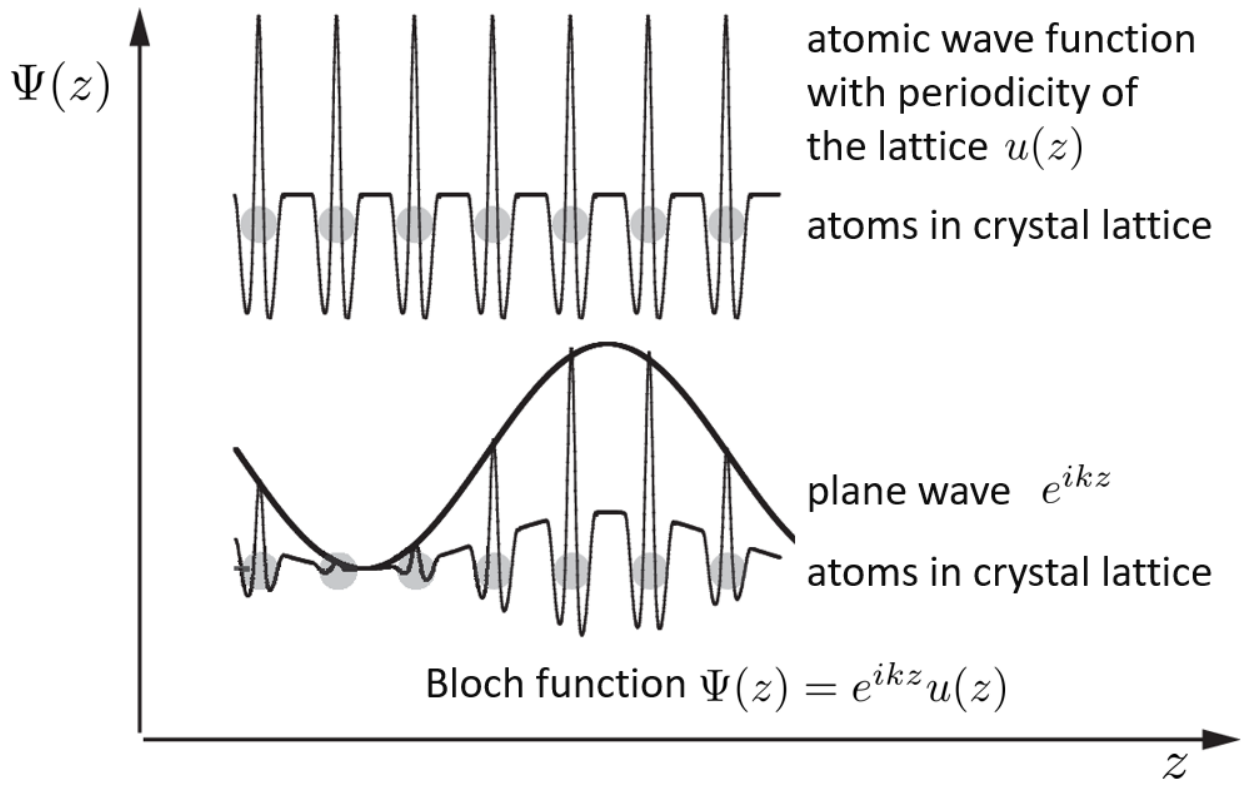


**Figure 2.8.:** Bloch functions are de Broglie-plane waves modulated in the pattern of the lattice. Graphic adapted from [39] .

The periodic nature from the real space transfers to the reciprocal space, since $\exp(i\mathbf{k}\mathbf{R}) = \exp(i(\mathbf{k}+\mathbf{G})\mathbf{R})$ for any reciprocal lattice vector $\mathbf{G}$, because $\exp(i\mathbf{G}\mathbf{R}) = \exp(i2\pi) = 1$. Therefore translation

by a reciprocal lattice vector in **k**-space gives us no new information. This enables us to focus on those values of **k**, which are enclosed by the primitive reciprocal lattice vectors instead of the full, infinite **k**-space. This confined region is called first Brillouin zone.

The energies of electronic states in **k**-space form continuous structures. Along a one-dimensional path in **k**-space these energies form bands. In figure 2.9, these energy bands are shown along a polygonal path between the high-symmetry **k**-points X, W, K, L, U, which are points on the border of the first Brillouin zone, and Γ, labeled G here, which is the centre of the Brillouin zone.

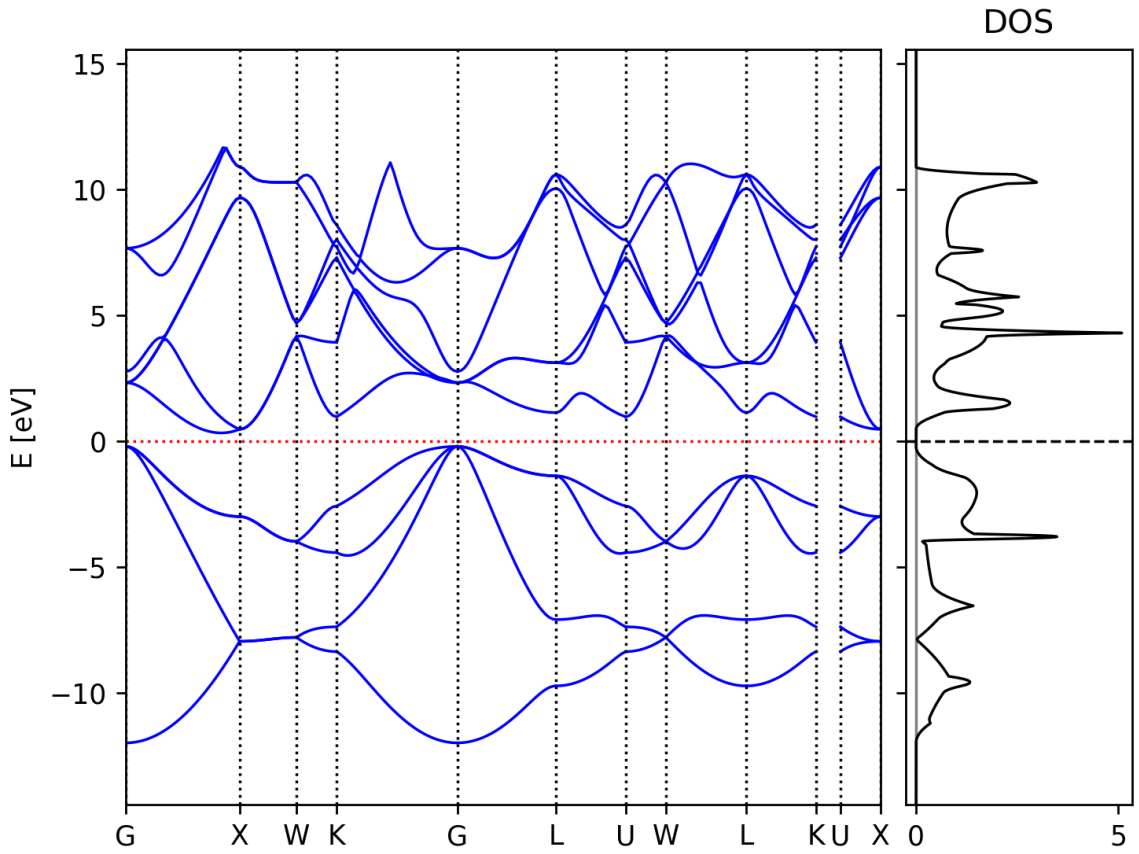


**Figure 2.9.:** Electronic band structure and density of states (DOS) of the primitive unit cell of diamond silicon with two atoms at 0K. The VBM is located at the Γ-point G; the CBM at approximately 85% of the distance from G to X. The dotted lines indicate the Fermi energy. All states below the Fermi energy are occupied at 0K; all states above it are unoccupied.

Only some of these electronic energy states in the crystal are actually occupied with electrons in the electronic ground state. The occupation probability is given by the Fermi distribution

$$f(\epsilon) = \frac{1}{1 + \exp(\frac{\epsilon - \epsilon_F}{k_B T})} \tag{2.32}$$

with the energy $\epsilon$, the temperature $T$, the Boltzmann constant $k_B$, and the Fermi energy $\epsilon_F$, which is implicitly defined by requiring that the sum over all occupation numbers adds up to then total number of electrons in the crystal. At 0K, all states below the Fermi energy are occupied, all states above are unoccupied. The Fermi energy is shown in figure 2.9 as a dotted line.

Completely filled and completely empty electronic bands cannot contribute a net current, as we explain in this paragraph. In quantum mechanics, a localised particle can be identified with a wave packet, which is traveling with the group velocity $\mathbf{v_k} = \frac{1}{\hbar}\nabla_{\mathbf{k}}\epsilon_{\mathbf{k}}$. The energies are symmetric to the center of the Brillouin zone for crystals with time-inversion symmetry: $\epsilon(\mathbf{k}) = \epsilon(-\mathbf{k})$. Evaluating the group velocities with the chain rule in electronic structures with the named symmetry shows that every group velocity $\mathbf{v_k}$ at $\mathbf{k}$ has a partner $-\mathbf{v_k}$ at $-\mathbf{k}$. The integral of the group velocity over the full Brillouin zone must thus vanish, if an energy band is fully occupied. Therefore there can be no net current, if all bands are fully occupied.

Conductors have partially occupied bands. In these partially occupied bands, the applied electric field causes a net change in crystal momentum, resulting in charge transport.

Semiconductors turn from insulators to conductors as their temperature increases. Semiconductors are isolators at 0K, but if the energy gap between the highest completely occupied band and the lowest empty band is small enough, electrons from the lower band can be excited by thermal energy to the higher band with sufficient probability. Given enough thermal energy in relation to the energy gap, the higher and lower band can be partially occupied according to the Fermi distribution. These partially occupied bands contribute to electronic transport, forming a semiconductor.

One of the most prominent semiconductors is silicon. Its electronic band structure with the band gap can be seen in figure 2.9. VBM and CBM are located at different $\mathbf{k}$-points, exhibiting an indirect band gap. For transitions between VBM and CBM, not only the transition energy must be provided, but also a crystal momentum, e.g. by a phonon.

With this electron-wave model applied to crystalline solids, we can thus understand why materials fall into three distinct categories with respect to their conductivity: insulators, semiconductors, and conductors, as we have seen in this section.

## 2.7. Boltzmann-Transport Equation

The Boltzmann-transport equation (BTE) delivers quantitative predictions of electrical conductivity.

The current density is $\mathbf{J} = n\mathbf{v}e$, where $n$ is the carrier density, $\mathbf{v}$ the mean carrier velocity and $e$ the elementary charge. To evaluate this formula, one must know: How many charge carriers have which velocity? Many electrons must be taken into account for any macroscopic current. It is better, not to look at so many particles individually, but at their phase-space distribution $f(\mathbf{r}, \mathbf{k}, t)$. How does the phase-space distribution change, when an external electric field is applied? Translating the formula for the current density into phase space, under the assumption that the phase-space distribution is homogeneous with respect to the position and time, it becomes:

$$\mathbf{J} = e \int \frac{d^3k}{(2\pi)^3} f(\mathbf{k}) \frac{\hbar \mathbf{k}}{m} \,, \tag{2.33}$$

where $\hbar$ is the reduced Planck's constant and $m$ the rest mass of the electron. Here and in the next paragraphs we follow Mahan's derivation [8] and continue to characterize the phase-space distribution $f(\mathbf{k})$ under the influence of an external electrical field $\mathbf{E}$.

The phase-space distribution $f(\mathbf{k})$ under the influence of an external electrical field $\mathbf{E}$ becomes stationary, if the shift rate of the distribution due to the electrical field equals the rate of change of the distribution due to collisions. We assume that the number of collisions is proportional to the difference between the phase-space distribution with and without electrical field.

$$\frac{-e\mathbf{E}}{\hbar} \cdot \nabla_{\mathbf{k}} f(\mathbf{k}) = \frac{f(\mathbf{k}) - f_0(\mathbf{k})}{\tau(\mathbf{k})} \,, \tag{2.34}$$

where $\tau(\mathbf{k})$ is the average time between collisions and $f_0$ is the phase-space distribution in equilibrium.

$\tau(\mathbf{k})$ can be calculated with Dirac's golden rule [40] (also known as Fermi's golden rule) as the average time between state transitions of an electron by interaction with a phonon in first-order perturbation theory [16]. Alternatively, it can be calculated with the Fan-Migdal electron self-energy in the self-energy relaxation approximation [41].

Rearranging the former equation for $f(\mathbf{k})$, we get:

$$f(\mathbf{k}) = f_0(\mathbf{k}) - \frac{e\mathbf{E}\tau(\mathbf{k})}{\hbar} \cdot \nabla_{\mathbf{k}} f(\mathbf{k}) \,. \tag{2.35}$$

Since $f(\mathbf{k})$ stands of both sides of the equation, it has to be solved iteratively. We can circumvent this by making the following approximation, which is valid as long as the non-equilibrium distribution does not differ too much from the equilibrium distribution:

$$f(\mathbf{k}) = f_0(\mathbf{k}) - \frac{e\mathbf{E}\tau(\mathbf{k})}{\hbar} \cdot \nabla_{\mathbf{k}} f_0(\mathbf{k}) \,. \tag{2.36}$$

The equilibrium phase-space distribution for electrons $f_0(\mathbf{k})$ is the Fermi function and thus analytically known. But the Fermi function informs about the occupation probability of an electronic state with a certain level of energy, while the input of the phase-space distribution is the crystal impulse $\mathbf{k}$. To make this compatible, the phase-space distribution is now interpreted as a function of energy, which itself is a function of the crystal impulse. With the chain rule, this leads to:

$$f(\mathbf{k}) = f_0(\mathbf{k}) - \frac{e\mathbf{E}\tau(\mathbf{k})}{\hbar} \cdot \underbrace{\nabla_{\mathbf{k}} \epsilon_{\mathbf{k}}}_{=\mathbf{v}_{\mathbf{k}}\hbar} \frac{\partial f_0}{\partial \epsilon_{\mathbf{k}}} \,. \tag{2.37}$$

Here, we use the abbreviation $\mathbf{v}_{\mathbf{k}} = \frac{1}{\hbar}\nabla_{\mathbf{k}}\epsilon_{\mathbf{k}}$, which is the group velocity of a wave packet that can be identified with a particle. We will now plug this expression into equation (2.33), which describes

the current density with the phase-space distribution, and immediately evaluate that the expected current without external field in equilibrium is zero. We get:

$$\mathbf{J} = -e^2 \int \frac{d^3k}{(2\pi)^3} \tau(\mathbf{k}) \mathbf{v}_\mathbf{k} (\mathbf{v}_\mathbf{k} \cdot \mathbf{E}) \frac{\partial f_0(k)}{\partial \epsilon_k} \,. \tag{2.38}$$

In Ohm's law $\mathbf{J} = \sigma \mathbf{E}$, $\sigma$ is a tensor of rank two in general, since $\mathbf{J}$ does not have to align with $\mathbf{E}$, but here we have assumed spatial homogeneity of the conductor, which implies isotropy. Thus we can now identify the electrical conductivity $\sigma$ as

$$\sigma = -e^2 \int \frac{d^3k}{(2\pi)^3} \tau(\mathbf{k}) \mathbf{v}_\mathbf{k}^2 \frac{\partial f_0(k)}{\partial \epsilon_k} \,. \tag{2.39}$$

This is a semiclassical model of the electron transport: classical, because the current is modelled as sum of velocities of classical particles; quantum mechanical, because the equilibrium phase-space distribution is chosen to be the Fermi distribution and the velocities of the particles are deduced from the energies in the band diagram, which emerges from a quantum mechanical model (see chapter 2.6).

The Boltzmann approach is widely used [16, 42–44]. In most cases, the calculation of carrier lifetime is based on the phonon picture in the harmonic approximation (see section 2.4). For harmonic materials, the BTE approach shows good agreement with experimental data [16]. For anharmonic materials, notable differences can be found. For example, Caruso's study of SnSe shows approximately 70% difference between the calculated electrical conductivity and the experiment at 300K (figure 3 in [44]). In the next chapter, we present the Kubo-Greenwood approach, which naturally includes all orders of potential anharmonicity.

## 2.8. Kubo-Greenwood Approach

This section is divided in three subsections: First, we show that the electrical conductivity can be deduced from the autocorrelation of the current density. Second, the reformulation of the autocorrelation, such that it can be evaluated on the basis of DFT results, is presented as the Kubo-Greenwood formula. Third, we display the workflow for the practical evaluation of the Kubo-Greenwood formula.

### 2.8.1. The Autocorrelation

The electrical conductivity can be deduced from the autocorrelation of the electrical current density. What is the response of the electron waves to an external electrical field? To deduce the electrical conductivity, we include the electric field into the Hamiltonian of the electron waves and determine the relation between expectation value of the current density operator on this electron waves and the electric field in first order, as shown by Zwanzig [10]:

The addition to the Hamiltonian caused by the electrical field is $H_1(t) = -\mathbf{E}(t)\mathbf{M}$, where $\mathbf{M}$ is the electrical polarisation and $\mathbf{E}(t)$ is the electrical field. Time-dependent perturbation theory yields the perturbed wavefunction :

$$\Psi(t) = \Psi_n \exp\left(-i\frac{\epsilon_n}{\hbar}t\right) + \sum_{m\neq n}\frac{1}{i\hbar}\int_0^t dt' \exp\left(i\frac{\epsilon_m-\epsilon_n}{\hbar}t'\right) < \Psi_m|H_1(t')|\Psi_n > \Psi_m \exp\left(-i\frac{\epsilon_m}{\hbar}t\right) + O(H_1^2)\,, \tag{2.40}$$

where $t$ is the time, $\Psi_m$ are the time-independent solutions of the undisturbed Schrödinger equation, $\epsilon_m$ are the eigenvalues to these solutions, and $\hbar$ is Planck's reduced constant.

To obtain the expectation value of the current-density operator, we will now build two different expectation values after each other. The first is the expectation value of an operator of a single quantum state, whose form depends on the basis that we chose for the representation of the quantum state. For example, if a spatial basis is chosen for the representation of the state $\Psi_n$, the expectation value $< \Psi_n|J_b|\Psi_m >= \int_{-\infty}^{+\infty}\int_{-\infty}^{+\infty}\int_{-\infty}^{+\infty} dxdydz\Psi_n^*(x,y,z)J_b\Psi_m(x,y,z)$ is an integral over space with $x, y, z$ Cartesian coordinates and the complex conjugate $\Psi_n^*$.

The first expectation value of the component $b$ of the current-density operator $\mathbf{J}$ is time-dependent as a result of the now time-dependent Hamiltonian:

$$\begin{aligned} < J_b(t) >=< \Psi_n|J_b|\Psi_n > &+ \sum_{m\neq n}\frac{1}{i\hbar}\int_0^t dt' < \Psi_n|J_b|\Psi_m > \exp\left(-i\frac{\epsilon_m-\epsilon_n}{\hbar}(t-t')\right) < \Psi_m|H_1(t')|\Psi_n > \\ &- \sum_{m\neq n}\frac{1}{i\hbar}\int_0^t dt' < \Psi_m|J_b|\Psi_n > \exp\left(-i\frac{\epsilon_n-\epsilon_m}{\hbar}(t-t')\right) < \Psi_n|H_1(t')|\Psi_m > \\ &+ O(H_1^2)\,, \end{aligned} \tag{2.41}$$

The second expectation is built over an ensemble of quantum states. In the thermodynamical equilibrium the occupation probability of an energy level is represented by the matrix elements of the density operator $< \Psi_m|\rho|\Psi_n >= \delta_{mn}\rho_n$ with $\rho_n = \exp(-\beta\epsilon_n)/\sum_n \exp(-\beta\epsilon_n)$ with $\beta = \frac{1}{k_B T}$, $T$ the

absolute temperature and $k_B$ the Boltzmann constant. Building the average over this ensemble , one obtains:

$$\begin{aligned} < J_b(t) >_{\text{ensemble}} = \underbrace{\sum_n \rho_n < \Psi_n|J_b|\Psi_n >}_{=0} + \int_0^t dt' \sum_{m\neq n}\sum_n \rho_n \frac{1}{i\hbar}\cdot \\ \cdot \Bigg[ < \Psi_n|J_b|\Psi_m > \exp\left(-i\frac{\epsilon_m - \epsilon_n}{\hbar}(t-t')\right) < \Psi_m|H_1(t')|\Psi_n > \\ - < \Psi_m|J_b|\Psi_n > \exp\left(-i\frac{\epsilon_n - \epsilon_m}{\hbar}(t-t')\right) < \Psi_n|H_1(t')|\Psi_m > \Bigg] \\ + O(H_1^2) \, , \end{aligned} \tag{2.42}$$

where the average current density vanishes in the undisturbed case in equilibrium.

We can now isolate the components of the electric field $E_a$ by replacing $H_1(t)$ with $-\mathbf{E}(t)\mathbf{M}$.

$$\begin{aligned} < J_b(t) >_{\text{ensemble}} = \int_0^t dt' \sum_n \sum_{m\neq n} \rho_n \frac{1}{i\hbar}\cdot \\ \cdot \Bigg[ < \Psi_n|J_b|\Psi_m > \exp\left(-i\frac{\epsilon_m - \epsilon_n}{\hbar}(t-t')\right) < \Psi_m| - M_a E_a(t')|\Psi_n > \\ - < \Psi_m|J_b|\Psi_n > \exp\left(-i\frac{\epsilon_n - \epsilon_m}{\hbar}(t-t')\right) < \Psi_n| - M_a E_a(t')|\Psi_m > \Bigg] \\ + O(H_1^2) \, . \end{aligned} \tag{2.43}$$

We emphasise that $\epsilon_m$ and $\epsilon_n$ are the eigenvalues of the undisturbed Schrödinger equation corresponding to energy values, while $E_a$ is the component of the electric field.

The spatially homogeneous electrical field can be pulled out of the expectation value:

$$\begin{aligned} < J_b(t) >_{\text{ensemble}} = \int_0^t dt' \sum_n \sum_{m\neq n} \rho_n \frac{1}{i\hbar}\cdot \\ \cdot \Bigg[ < \Psi_n|J_b|\Psi_m > \exp\left(-i\frac{\epsilon_m - \epsilon_n}{\hbar}(t-t')\right) < \Psi_m| - M_a|\Psi_n > \\ - < \Psi_m|J_b|\Psi_n > \exp\left(-i\frac{\epsilon_n - \epsilon_m}{\hbar}(t-t')\right) < \Psi_n| - M_a|\Psi_m > \Bigg] E_a(t') \\ + O(E_a(t')^2) \, . \end{aligned} \tag{2.44}$$

The blue part can now be identified with the transfer function, which contains all information of the linear response, since it satisfies $< J_b(t) >_{\text{ensemble}} = < J_b >_{\text{ensemble}} + \int_0^t dt' \Phi_{ba}(t-t') E_a(t') + O(E_a^2)$:

$$\Phi_{ba}(t-t') = \sum_n \sum_{m \neq n} \rho_n \frac{1}{i\hbar} \cdot \Bigg[ < \Psi_n | J_b | \Psi_m > \exp\left(-i \frac{\epsilon_m - \epsilon_n}{\hbar}(t-t')\right) < \Psi_m | - M_a | \Psi_n > \\ - < \Psi_m | J_b | \Psi_n > \exp\left(-i \frac{\epsilon_n - \epsilon_m}{\hbar}(t-t')\right) < \Psi_n | - M_a | \Psi_m > \Bigg] . \tag{2.45}$$

From here onwards we will focus solely on the transfer function, whose Fourier transform can be identified with the frequency-dependent alternating-current conductivity. We seize the opportunity to simplify $\Phi_{ba}(t-t')$ slightly by renaming it into $\Phi_{ba}(t)$. Pulling out the minus in front of $M_a$, inverts the order of minuend and subtrahend

$$\Phi_{ba}(t) = \sum_n \sum_{m \neq n} \rho_n \frac{1}{i\hbar} \cdot \Bigg[ < \Psi_m | J_b | \Psi_n > \exp\left(i \frac{\epsilon_m - \epsilon_n}{\hbar} t\right) < \Psi_n | M_a | \Psi_m > \\ - < \Psi_n | J_b | \Psi_m > \exp\left(i \frac{\epsilon_n - \epsilon_m}{\hbar} t\right) < \Psi_m | M_a | \Psi_n > \Bigg] . \tag{2.46}$$

The time-independent matrix elements of the current density can be substituted with the time-dependent ones by $< \Psi_m | \mathbf{J} | \Psi_n > \exp(i \frac{\epsilon_m - \epsilon_n}{\hbar} t) = < \Psi_m | \mathbf{J}(t) | \Psi_n >$, which gives us:

$$\Phi_{ba}(t) = \sum_n \sum_{m \neq n} \rho_n \frac{1}{i\hbar} \cdot \Bigg[ < \Psi_m | J_b(t) | \Psi_n > < \Psi_n | M_a | \Psi_m > \\ - < \Psi_n | J_b(t) | \Psi_m > < \Psi_m | M_a | \Psi_n > \Bigg] . \tag{2.47}$$

Evaluating Heisenberg's equation of motion for the operator $\mathbf{M}$, $< \Psi_m | \mathbf{M} | \Psi_n >$ can be replaced with its time derivative by $< \Psi_m | \mathbf{M} | \Psi_n > = < \Psi_m | d/dt \mathbf{M} | \Psi_n > \frac{-i\hbar}{\epsilon_m - \epsilon_n}$, where $< \Psi_m | d/dt \mathbf{M} | \Psi_n >$ can in turn be replaced with the current density multiplied with the system's volume $< \Psi_m | \mathbf{J} V | \Psi_n >$. This yields

$$\Phi_{ba}(t) = \sum_n \sum_{m \neq n} \rho_n \Bigg[ < \Psi_n | J_b(t) | \Psi_m > < \Psi_m | J_a V | \Psi_n > \frac{1}{\epsilon_m - \epsilon_n} \\ - < \Psi_m | J_b(t) | \Psi_n > < \Psi_n | J_a V | \Psi_m > \frac{1}{\epsilon_n - \epsilon_m} \Bigg] . \tag{2.48}$$

The second sum is not running over $m = n$. To reach a more compact analytical expression, we want to include $m = n$ in the second sum, but the term $\frac{1}{\epsilon_n - \epsilon_m}$ diverges in that case. However, we can cure this problematic term, if we can bring in a nominator that approaches zero more rapidly. Interpretating the closely spaced discrete differences $\epsilon_n - \epsilon_m$ as a continuous variable $\Delta$, such a denominator can be found in $\exp(\beta\Delta) - 1$, which can be produced by extending with the occupation probability $\frac{\rho_m}{\rho_m}$. Applying the rule of Bernoulli and l'Hospital

$$\lim_{\Delta \to 0} \frac{\frac{d}{d\Delta}(\exp(\beta\Delta) - 1)}{\frac{d}{d\Delta}\Delta} = \lim_{\Delta \to 0} \frac{\beta \exp(\beta\Delta)}{1} = \beta \Rightarrow \lim_{\Delta \to 0} \frac{\exp(\beta\Delta) - 1}{\Delta} = \beta \ , \tag{2.49}$$

we see that the problematic fraction has now become a legit term, which can be included by adding and immediately subtracting $\sum_n \rho_m < \Psi_n | J_b(t) | \Psi_n > < \Psi_n | J_a V | \Psi_n > \frac{1}{\epsilon_n - \epsilon_n} \frac{\rho_n}{\rho_m}$. The added term removes the exclusion $m \neq n$ in the first part of the sum, while the subtracted one effects the same in the second part:

$$\begin{aligned} \Phi_{ba}(t) = & \sum_m \sum_n \rho_m < \Psi_m | J_a V | \Psi_n > < \Psi_n | J_b(t) | \Psi_m > \frac{1}{\epsilon_m - \epsilon_n} \frac{\rho_n}{\rho_m} \\ & - \sum_n \sum_m \rho_n < \Psi_n | J_a V | \Psi_m > < \Psi_m | J_b(t) | \Psi_n > \frac{1}{\epsilon_n - \epsilon_m} \ . \end{aligned} \tag{2.50}$$

We can now rename the indices in the second double sum $n \to m$ and $m \to n$ and see that both sums are the same, except for the factor $\frac{\rho_n}{\rho_m} = \exp(-\beta(\epsilon_n - \epsilon_m))$. A more concise notation is thus:

$$\Phi_{ba}(t) = \sum_m \sum_n \rho_m < \Psi_m | J_a V | \Psi_n > < \Psi_n | J_b(t) | \Psi_m > \frac{1}{\epsilon_m - \epsilon_n} \left[ \exp(-\beta(\epsilon_n - \epsilon_m)) - 1) \right] \ . \tag{2.51}$$

After extending with $\frac{\beta}{\beta}$, parts of this expression can be rewritten as the Kubo transform $\tilde{J}_a$

$$\frac{1}{\beta} < \Psi_m | J_a V | \Psi_n > \frac{\exp(-\beta(\epsilon_n - \epsilon_m)) - 1}{\epsilon_m - \epsilon_n} = \tilde{J}_a = \frac{1}{\beta} \int_0^\beta d\lambda \exp(\lambda H) J_a \exp(-\lambda H) \ . \tag{2.52}$$

With this replacement and applying the definitions of matrix multiplication and the ensemble average, the autocorrelation in the transfer function becomes apparent:

$$\Phi_{ba}(t) = \beta V < \tilde{J}_a J_b(t) >_{\text{ensemble}} \ . \tag{2.53}$$

The temporal transfer function can be converted into the frequency response with the Fourier transform, for which we can start the integration at 0 instead of the usual $-\infty$, because $\mathbf{J}$ gives only zero contribution for negative $t$, since $\mathbf{E}$ is switched on at $t = 0$, yielding the frequency-dependent conductivity

$$\sigma_{ba}(\omega) = \int_0^\infty dt \exp(-i\omega t) \Phi_{ba}(t) \ . \tag{2.54}$$

In this way, the electrical conductivity can be related to the autocorrelation of the electrical current density, as derived above.

The autocorrelation function of the current density can be obtained from the equilibrium. An external electrical field is not needed. The current density in equilibrium is zero averaged over longer periods of time, but it shows instantaneous nonzero fluctuations from one moment to the other. This is known as Johnson noise [45]. The finite electrical conductivity, on the other hand, is a result of dissipation. Hence the expression of electrical conductivity in terms of the autocorrelation can be seen as an instance of the fluctuation-dissipation theorem connecting equilibrium and non-equilibrium.

The fluctuating current density in equilibrium can be represented as a superposition of periodic oscillations. The autocorrelation preserves the periodicity of its input signal. Therefore periodic oscillations contained in the fluctuating current density are also present in the autocorrelation. According to the last equation, the electrical conductivity $\sigma_{ba}(\omega)$ is the highest for the oscillations most present in the autocorrelation. This reveals an intuitively satisfying relation: The system shows higher conductivities for external stimuli at frequencies, which are naturally more likely to appear in the system as fluctuations without an external field.

### 2.8.2. The Kubo-Greenwood Formula

The autocorrelation function can be computed via DFT. This is important for the practical applicability. In this section, we sketch, how the abstract autocorrelation formula is transformed by Holst et al. [11], such that it can be evaluated on the basis of DFT results.

First, the total current-density operator is rewritten in second quantisation:

$$J_a = \frac{1}{V} \sum_{\mathbf{k}\mathbf{k}'\nu\mu} |\langle \mathbf{k}\mu | \frac{e}{m} \mathbf{p} | \mathbf{k}'\nu \rangle| a^\dagger_{\mathbf{k}\mu} a_{\mathbf{k}'\nu} \ , \tag{2.55}$$

where $a^\dagger_{\mathbf{k}\mu}$ is the creation operator of the electron state $|\mathbf{k}\mu\rangle$ characterised by its band index $\mu$ and its crystal impulse $\mathbf{k}$ and $a_{\mathbf{k}'\nu}$ is the annihilation operator with an analogous characterisation. $e$ is the elementary charge, $m$ the mass of the electron and $\mathbf{p}$ the impulse operator of a single electron.

Second, the ensemble average over creation and annihilation operators is expressed with Fermi functions $f_{\mu\mathbf{k}} = (1 + \exp(\beta(\epsilon_{\mu\mathbf{k}} - \epsilon_F)) + 1)^{-1}$ with the Fermi energy $\epsilon_F$ and Kronecker's $\delta_{\mu\tau}$ by Wick's theorem

$$\mathrm{Tr}(\rho a^\dagger_{\mathbf{k}\mu} a_{\mathbf{k}'\nu} a^\dagger_{\mathbf{l}\lambda} a_{\mathbf{l}'\tau}) = f_{\mu\mathbf{k}} \delta_{\mathbf{k}\mathbf{k}'} \delta_{\mu\nu} f_{\lambda\mathbf{l}} \delta_{\mathbf{l}\mathbf{l}'} \delta_{\mu\tau} + f_{\mu\mathbf{k}} \delta_{\mathbf{l}'\mathbf{k}} \delta_{\mu\tau} (1 - f_{\lambda\mathbf{l}}) \delta_{\mathbf{l}\mathbf{k}'} \delta_{\lambda\nu} \ . \tag{2.56}$$

With that, the integrals over time in the Fourier-Transform (eq. 2.54) and over inverse energy in the Kubo-Transform (eq. 2.52) can be carried out, leading to the final expression for the Onsager coefficient $L_{11}$, which can be identified with the electrical conductivity

$$L_{11}(\omega) = \frac{2\pi e^2}{3Vm^2\omega} \sum_{\mathbf{k}\nu\mu} |\langle \mathbf{k}\nu | \mathbf{p} | \mathbf{k}\mu \rangle|^2 (f_{\mathbf{k}\nu} - f_{\mathbf{k}\mu}) \delta(\epsilon_{\mathbf{k}\mu} - \epsilon_{\mathbf{k}\nu} - \hbar\omega) \ . \tag{2.57}$$

The factor $\frac{1}{3}$ is added in account for averaging over all three spatial directions. The electronic states $|\mathbf{k}\mu\rangle$ include the lattice dynamics to all orders, since they are computed for nuclear geometries of uncorrelated snapshots of molecular-dynamics trajectories. Averaging $L_{11}$ over uncorrelated snapshots implements the thermodynamical ensemble average.

Next, we want to illustrate the Kubo-Greenwood formula for the Onsager coefficient $L_{11}$, which we will focus on for the rest of this thesis (see figure 2.10).

For each value $L_{11}(\omega)$ at a certain frequency $\omega$, a sum over all $\mathbf{k}$-points is computed. A non-zero contribution at a $\mathbf{k}$-point can be found under three conditions: First, there must be a difference in the energy levels $\epsilon_{\mathbf{k}\mu} - \epsilon_{\mathbf{k}\nu}$ at this $\mathbf{k}$-point that equals the energy $\hbar\omega$ of a photon of frequency $\omega$, which is an oscillating electrical field. Second, there must be a difference in the electronic occupation of these energy levels. Third, the expectation value of the momentum matrix elements must not be vanishing.

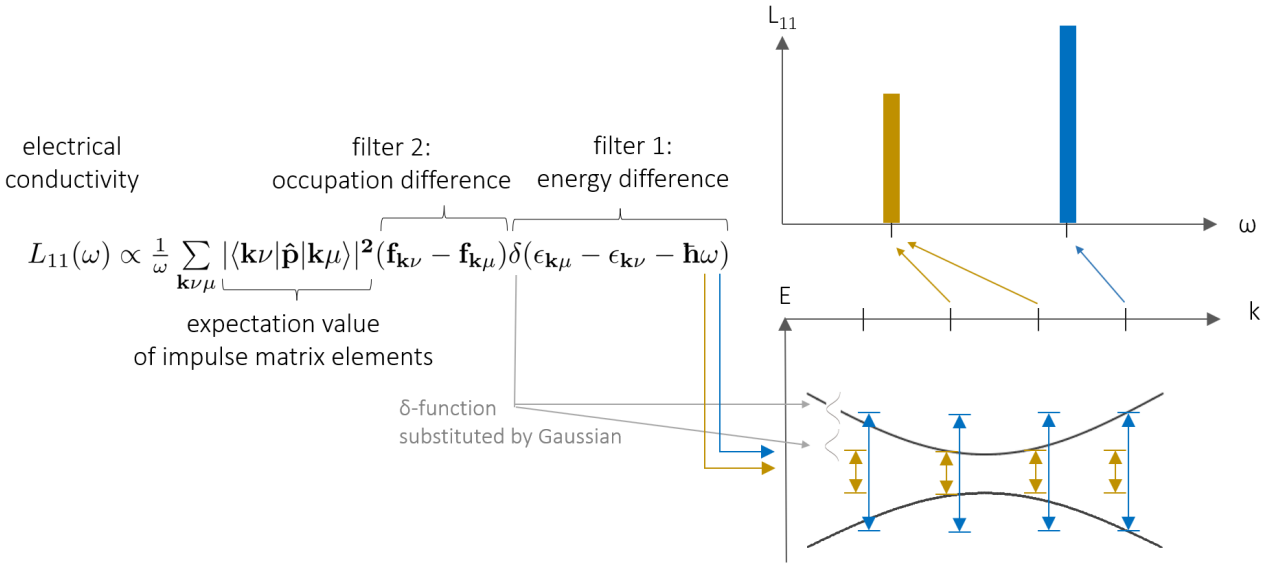


**Figure 2.10.:** Every $\mathbf{k}$-point can contribute to $L_{11}$ at all frequencies $\omega$. At every $\mathbf{k}$-point the energy differences between all electronic energies are checked for a matching transition corresponding to the energy of a photon $\hbar\omega$. By replacing the $\delta$-function by a Gaussian of a certain width, one adds a tolerance to this matching. Matching energies contribute proportional to the their difference in the occupation probability and expectation value of their momentum matrix elements.

The second condition is fulfilled for all transitions between completely filled and empty states and for transitions between partially occupied states. The transitions between completely occupied and empty states in semiconductors have an energy difference that is greater or equal to the band gap energy. These transitions we call interband transitions. For the prediction of electrical conductivity, we are not interested in these interband transitions, but in the intraband transitions, which occur due to supercell folding of the band diagram.

For the small $\omega$-values of interest below the interband transition energies, the second condition is fulfilled only for energies close to the highest occupied state and the lowest unoccupied state, because only here thermal excitation is possible at room temperature. We can thus focus on an

energy window around the band gap as validated in section 3.3. Concerning the first condition, we remark, that for the numerical implementation in the computer Dirac's $\delta$-function must be approximated. Options, among others, are a Gaussian or a Lorentzian function with small widths. We opted for the Gaussian and use it throughout this thesis.

The use of a broadening function is necessary, since only a finite number of $\omega$-points for photonic energies $\hbar\omega$ and a finite number of electronic energies over **k**-space can be sampled in practise, even though both energies theoretically provide a continuous spectrum. The probability for an exact match between the energy $\hbar\omega$ and the band-energy differences is thus vanishingly small in numerical calculations. A replacement function with a nonzero width introduces a tolerance for this match and is thus numerically favourable.

Let us now discuss the influence of a more dispersive electronic band diagram: If the band structure is more dispersive (see figure 2.11), fewer electronic states are sampled in the important region with free charge carriers around the VBM and CBM (bordered by the blue lines). Thus a more dispersive electronic band structure demands higher **k**-grid densities for achieving reliable results.

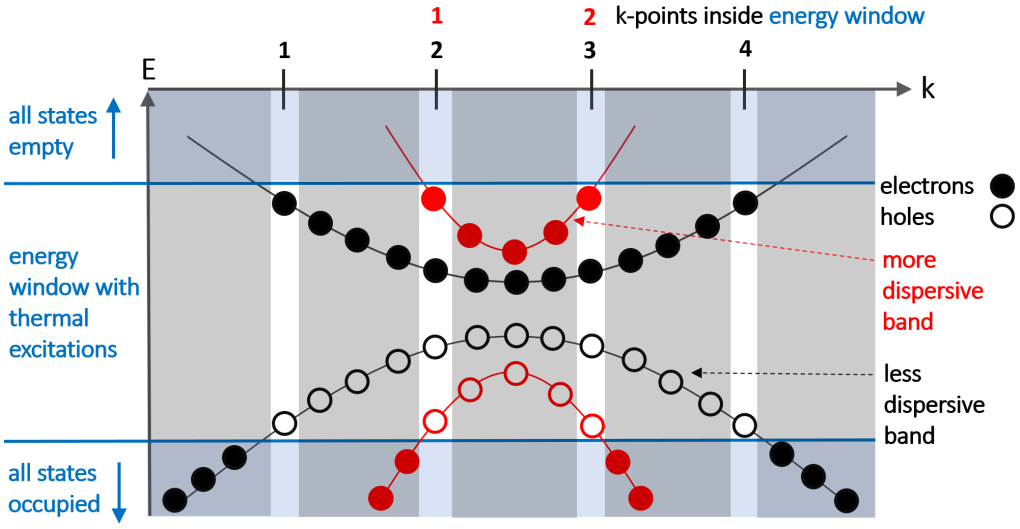


**Figure 2.11.:** Electronic band diagram as shown in figure 2.10, but now with a very simple configuration of occupation and in comparison with more dispersive bands (red). Here, all electrons in the valence band above a certain energy level (lower blue line) are assumed to be thermally excited to the conduction band. This discrete behaviour is a simplification for clarity's sake. In reality, the occupation probability is given by the Fermi function. The transparent grey background indicates regions, in which no **k**-points are sampled and consequently no contributions to the Kubo-Greenwood formula are registered. The transparent blue background shows regions, in which no free carriers are present and thus no contributions to conductivity are given. The possibly contributing states are thus highlighted with a white background. While four **k**-points are sampling the electronic states of the less dispersive material (black) in the contributing region around the band gap, only two **k**-points map the contributing electronic states of the more dispersive material (red). A less reliable $L_{11}$ is the consequence for the more dispersive band structure. Thus higher **k**-grid densities are needed for materials with more dispersive band structures.

### 2.8.3. The Kubo-Greenwood Workflow

The workflow of the Kubo-Greenwood approach consists of the following four steps (see figure 2.12): First, a MD trajectory on the full potential energy surface (PES) is computed. Second, uncorrelated snapshots of momentaneous configurations are extracted from this trajectory. The time interval is chosen such that the autocorrelation among single snapshots is below a vanishing, upper limit as we want to have an ensemble of samples, which are independent from each other. In this work, however, we generated the uncorrelated snapshots with harmonic sampling to save computational costs (see section 3.1). Third, the electronic band structure of the momentaneous configurations is computed and the transport spectra of the Onsager coefficients are formed on the basis of the electronic structure via the Kubo-Greenwood formula for each snapshot as explained in the previous section.

Finally, the thermodynamical average over all single snapshot spectra is computed. From this average spectrum the direct-current conductivity at zero frequency can be extrapolated (see section 3.6).

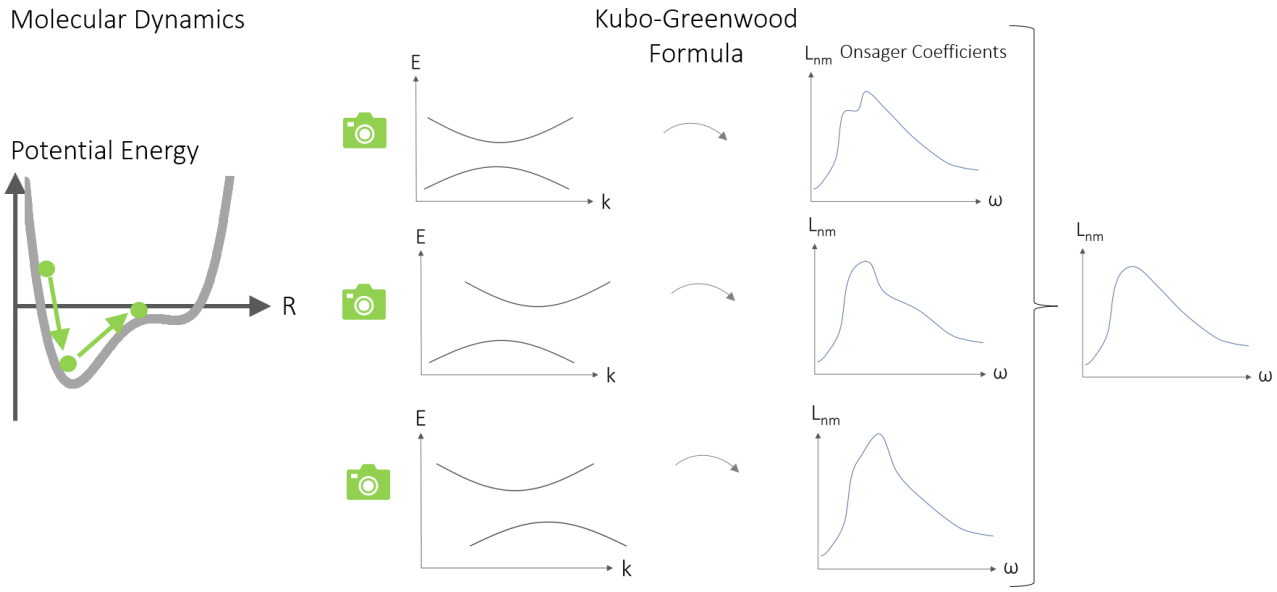


**Figure 2.12.:** Schematic sketch of the Kubo-Greenwood workflow from left to right: A MD trajectory is computed, from which snapshots of momentaneous configurations are excerpted. The electronic band structure of the momentaneous configurations is computed and the transport spectra of the Onsager coefficients are formed on the basis of the electronic band diagrams via the Kubo-Greenwood formula for each snapshot. Finally, the thermodynamical average over all single snapshot spectra is computed. From this average spectrum the direct-current conductivity at zero frequency can be extrapolated (see section 3.6).

# 3. Results

The Kubo-Greenwood method is an appealing alternative to perturbative approaches, since it naturally incorporates all orders of anharmonicity. However, its computational costs can be prohibitively high for regular crystals. One key cost factor is the **k**-grid sampling.

In the following, we investigate the effect of the **k**-grid density on the transport spectrum in detail with respect to convergence and computational costs. First, we describe the generation of the investigated thermodynamical ensemble by harmonic sampling. Second, we discuss the convergence of our results with respect to the sampling rate in frequency space, the broadening parameter, and the chosen energy window. Furthermore, we investigate the **k**-grid convergence of the $L_{11}$ spectrum of silicon and discuss the origin of the large, associated computational cost. After that, we show how the Fourier interpolation can substantially reduce the computational costs and demonstrate, how this enables quantitative convergence of the **k**-grid spectrum. After having converged the spectrum of a single sample with respect to the **k**-grid, we analyse the convergence of the averaged $L_{11}$ over a thermodynamical ensemble. This then allows an extrapolation of the conductivity and mobility to the direct-current limit.

The results are computed on the supercomputer Cobra of the Max-Planck-Computing-and-Data-Facility (MPCDF). A regular node on Cobra has 40 cores and a memory of 96GB.

All computations are performed with FHI-aims [28] in the local density approximation without spin-orbit coupling, but including relativistic effects. The light basis set of Si is used. Convergence tests for the basis set in [46] revealed that the light basis is sufficient. The broadening scheme for the occupation of the Kohn-Sham eigenstates is the Fermi function at 300K.

## 3.1. Harmonic Sampling

For harmonic materials, it is convenient to perform thermodynamic averages using the harmonic Hamiltonian, since this saves the cost of a MD simulation. For silicon, which is indeed a very harmonic material, this is a justified approximation.

We can exploit this for the generation of a thermodynamical ensemble needed for the Kubo-Greenwood approach. Instead of generating the ensemble from snapshots of a cost intensive MD trajectory, we can displace the atoms from their equilibrium position according to the harmonic approximation, the equation of motion of which can be solved analytically (see section 2.4).

In the phonon particle picture, we can occupy the modes due to the Boltzmann or the Bose-Einstein distribution, which correspond to the classical and quantum mechanical occupation statistics respectively. For Si, it is necessary to use the Bose-Einstein distribution, because the specific heat of silicon is still strongly temperature dependent at 300K [47], indicating the need to include

quantum nuclear effects. Classically, employing the Boltzmann distribution, one expects temperature independence of the specific heat.[1] Including quantum-nuclear effects in a MD calculation would require additional efforts, e.g., performing quantum-nuclear path-integral MD [48, 49] or the usage of colored thermostats [50]. To save these additional efforts, is a supplementary advantage of harmonic sampling, since we can directly occupy the modes according to the Bose-Einstein distribution (see section 2.4). We opt for harmonic sampling with FHI-vibes due to the harmonic nature of silicon and the quickness of this method.

Nevertheless, it must clearly be pointed out, that anharmonicities are thereby neglected. Despite this, we have decided for harmonic sampling for four reasons: 1) We save computational time. 2) The difference in results should be small since Si is a very harmonic material. 3) We can occupy the phonon modes according to the Bose-Einstein distribution. 4) The main goal of this thesis is the demonstration of **k**-grid convergence. Once the **k**-point convergence is demonstrated, the harmonic samples can easily be replaced with snapshots from MD simulation in further work to include anharmonicities.

All results in this thesis are calculated from geometries, which were generated by harmonic sampling. To this end, we relaxed the unit cell and computed converged phonon bands and force constants via phonopy/FHI-vibes[33, 34]. After these preparations, we generated 90 harmonic samples of 64 Si atoms in a cubic unit cell at 300K using the Bose-Einstein distribution.

## 3.2. The $\omega$-sampling

The angular frequency $\omega$ describes the frequency of an alternating electrical field. The conductivity $\sigma(\omega)$ characterises the material's linear charge-transport response to this alternating electrical field. We focus on frequencies relevant for the direct-current conductivity estimation, i.e. frequencies associated with intraband contributions in the low-frequency regime (red rectangle in figure 3.1). The $\omega$-sampling rate and postprocess-broadening width should be chosen such that they densely cover the transition energy spectrum, as we explain in this section.

The $L_{11}$ intensities are calculated for specific $\omega$-points. The $\omega$-points are chosen equidistantly in a specified energy interval with a specified frequency of the sampling. A spectrum consisting of discrete $\omega$-points with a certain, fixed distance between each other is the consequence.

More $\omega$-points lead to more computational costs, since the Kubo-Greenwood formula (2.57) is evaluated at each $\omega$-point. Only a certain energy interval around each $\omega$-point can give nonzero contributions to the $L_{11}$ spectrum, since the Kubo-Greenwood formula (2.57) contains Dirac's $\delta$-function and this $\delta$-function is modeled with a finite-width Gaussian, as discussed in subsection 2.8.2. The thereby introduced tolerance smears out 68% of the $L_{11}$ intensities over one standard deviation of the Gaussian and 95% over two standard deviations. This smoothening allows to use a relatively coarse $\omega$-spacing. However, a problem arises, when only so few $\omega$-points are chosen, that

1 The specific heat is the rate of change of the inner energy $U$ of a solid with respect to its temperature $T$, while keeping its volume $V$ constant: $(\frac{\partial U}{\partial T})_{V=const}$. Classically, one expects for such large systems like solids an inner energy of $\approx 3Nk_BT$, with $N$ the number of atoms and $k_B$ Boltzmann's constant. The result is a constant, expected, specific heat [35].

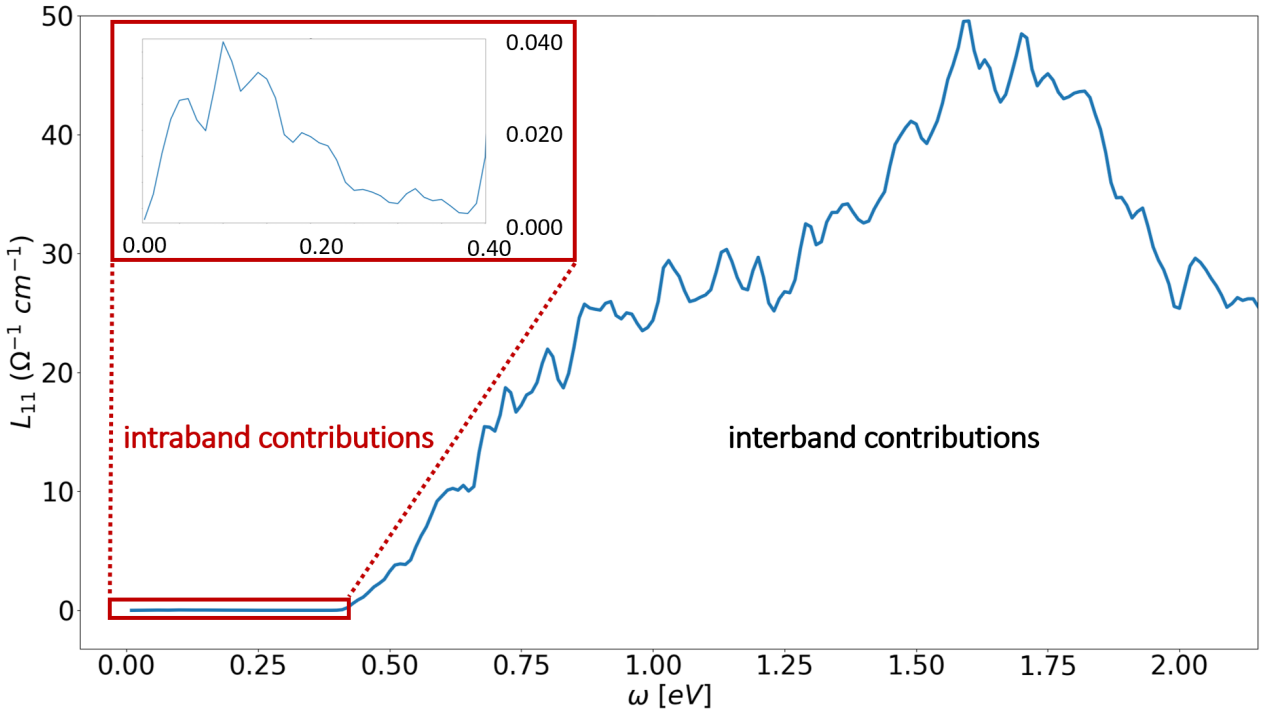


**Figure 3.1.:** $L_{11}$ spectrum of single sample of 64 Si atoms at 300K is shown with small intraband contributions on the left-hand side, which are meaningful for the direct-current conductivity prediction, and large interband contributions on the right-hand side, which can be discarded for the direct-current conductivity prediction.

the Gaussians around them do not have an overlap that is significantly different from zero. In these regions, the calculation is blind for $L_{11}$ contributions, which can lead to a serious distortion of the resulting spectrum. This can be seen clearly in the following toy spectrum (figure 3.2). Here we chose an extremely small broadening and fewer **k**-points than usual to illustrate this point: The peak on the left is not detected at all by the orange curve representing an $\omega$-step 10 times larger than the Gaussian broadening. All other curves, whose $\omega$-steps are equal or smaller than the broadening register this contribution. The peak on the right, however, is detected by the orange curve as well, since it happens to be close enough to a sampling point of the orange curve. Additionally, we see that the green curve has the highest values at both peaks. The reason for that is that the blue and magenta curve with their wider Gaussians are smearing out the contribution over a larger frequency interval. One can now argue, that a large width of the Gaussian makes it easy to cover the investigated spectrum with only a few $\omega$-points sufficiently, but the Gaussian should be as narrow as possible as it is a replacement for the infinitely narrow Dirac $\delta$-function in equation (2.57), as discussed in section 3.5.

The goal is thus to choose the smallest number of $\omega$-points that is still delivering a representative spectrum. In order to do so, we choose the number of $\omega$-points as a function of the Gaussian width, i.e., all $\omega$-points exactly one standard deviation apart. The resulting orange curve with a Gaussian broadening of 10meV and a $\omega$-sampling of 10meV captures the local minima and maxima almost as accurately as the blue curve with a broadening of 10meV and a $\omega$-sampling of 1meV as shown in figure 3.3. The green curve with a broadening of 10meV and a $\omega$-sampling of 100meV, on

the other hand, misses these local extrema. Thus the sampling of $\omega$-points provides a reasonable balance between representativeness of the spectrum and computational costs. Especially for the ensemble averages, for which single-sample inaccuracies cancel out (see section 3.7), we will stick to this guideline throughout this thesis. For single-sample computations however, we sometimes increase the number of $\omega$-points to present smoother curves, which are more pleasant to the reader's eye.

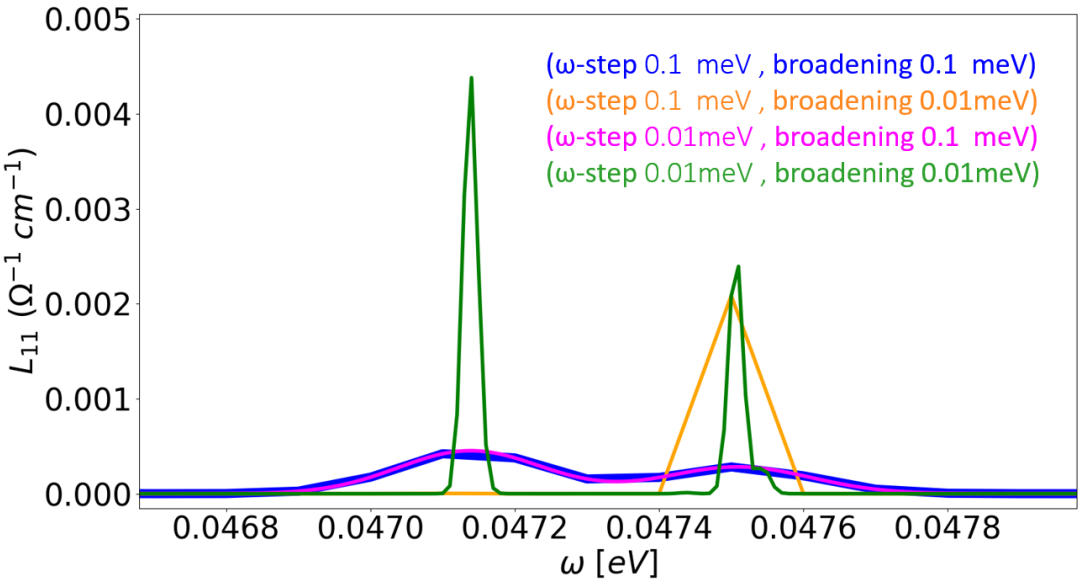


**Figure 3.2.:** Comparison of the $L_{11}$ spectrum of single sample of 64 Si atoms at 300K for different $\omega$-resolutions at an 8x8x8 **k**-grid with 512 **k**-points for very fine combinations of Gaussian broadening and $\omega$-steps. All possible four combinations of $\omega$-steps {0.1meV, 0.01meV} and Gaussian broadening {0.1meV, 0.01meV} are shown to illustrate the blindness for some relevant contributions that come with an $\omega$-steps that is far larger than the Gaussian broadening.

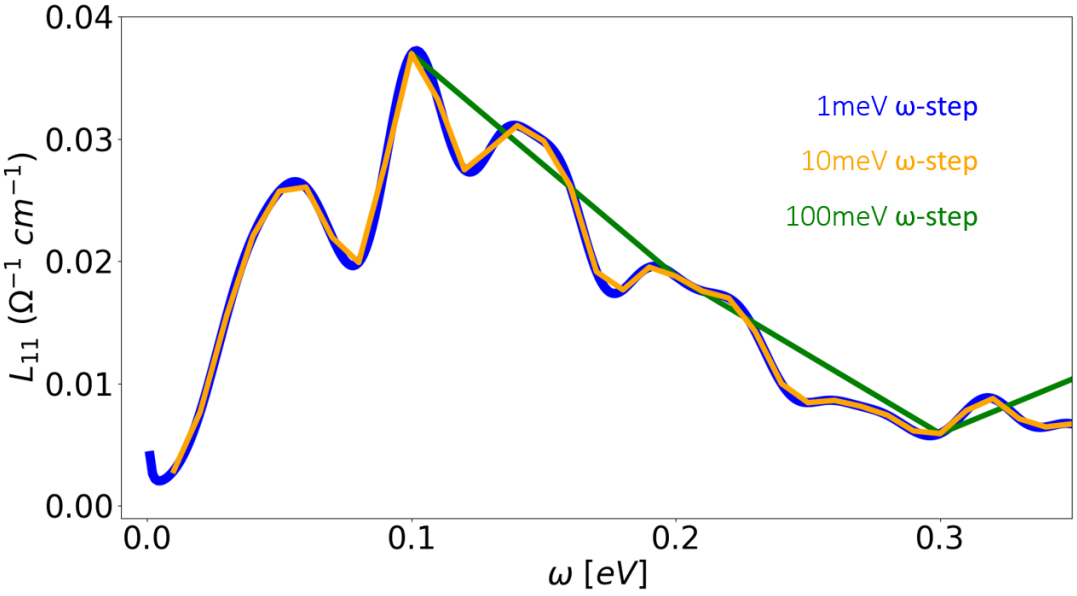


**Figure 3.3.:** Comparison of the $L_{11}$ spectrum of single sample of 64 Si atoms at 300K for different $\omega$-resolutions at a 16x16x16 **k**-grid with 4096 **k**-points for the same Gaussian broadening of 10meV. The orange curve with an $\omega$-step of 10meV captures all the local minima and maxima, which are also displayed by the blue curve with an $\omega$-step of 1meV. These local extrema are missed by the green curve with an $\omega$-step of 100meV.

## 3.3. The Energy Window

The evaluation of the Kubo-Greenwood formula (2.57) can be restricted to electronic states within a specified energy range to save computational costs. The specified energy range is called energy window.

The investigated energy window of the electronic band diagram should be as narrow as possible to save computational costs, but still capture all states with fractional occupation numbers. Since the majority of electronic states are either completely occupied or completely empty, they will not contribute to the $L_{11}$ intensities in the low-frequency, intraband regime (see figure 3.1 in section 3.2). Thus we can exclude these regions of the electronic structure from our calculations to reduce computational costs, as these regions yield zero contributions to the Kubo-Greenwood formula (2.57) in the low-frequency regime. The task is now to determine the minimal energy window, which still includes all electronic states relevant to the low frequencies of the $L_{11}$ spectrum.

To accomplish that, we first looked up the energy levels and occupation numbers at the Γ-point to get a rough estimate of the energies with fractional occupation number. After that, we fix one border of the energy window with a safety margin of a few 100meV with respect to the highest (respectively lowest) energy level with a fractional occupation number at the Γ-point. This is a large safety margin considering that the the thermal energy $k_BT$ is ≈ 26meV and the occupation probability decays exponentially with $\frac{\epsilon-\epsilon_F}{k_BT}$ according to the Fermi distribution. Thereafter we vary the other border of the energy window in steps of 100meV to determine an appropriate energy window.

Choosing an energy window with an upper boundary above $\epsilon_{max}$ = -5.2eV, which is 190meV over the CBM, does not change the $L_{11}$ spectrum anymore (figure 3.4). The same holds true for a lower boundary of $\epsilon_{min}$ = -6.0eV (figure 3.5), which is 250meV under the VBM. Since the VBM and CBM fluctuate with nuclear displacements, one should include a safety margin in practise. We thus choose an energy window between $\epsilon_{max}$ = -4.6eV and $\epsilon_{min}$ = -6.2eV to run our calculations. We decided for a larger safety margin on the upper boundary, because at higher frequencies around $\omega$ = 1eV in the realm of interband transitions, as displayed in figure 3.1, the convergence for the upper boundary was much slower than for the lower boundary. We stick to this energy window for the course of this thesis.

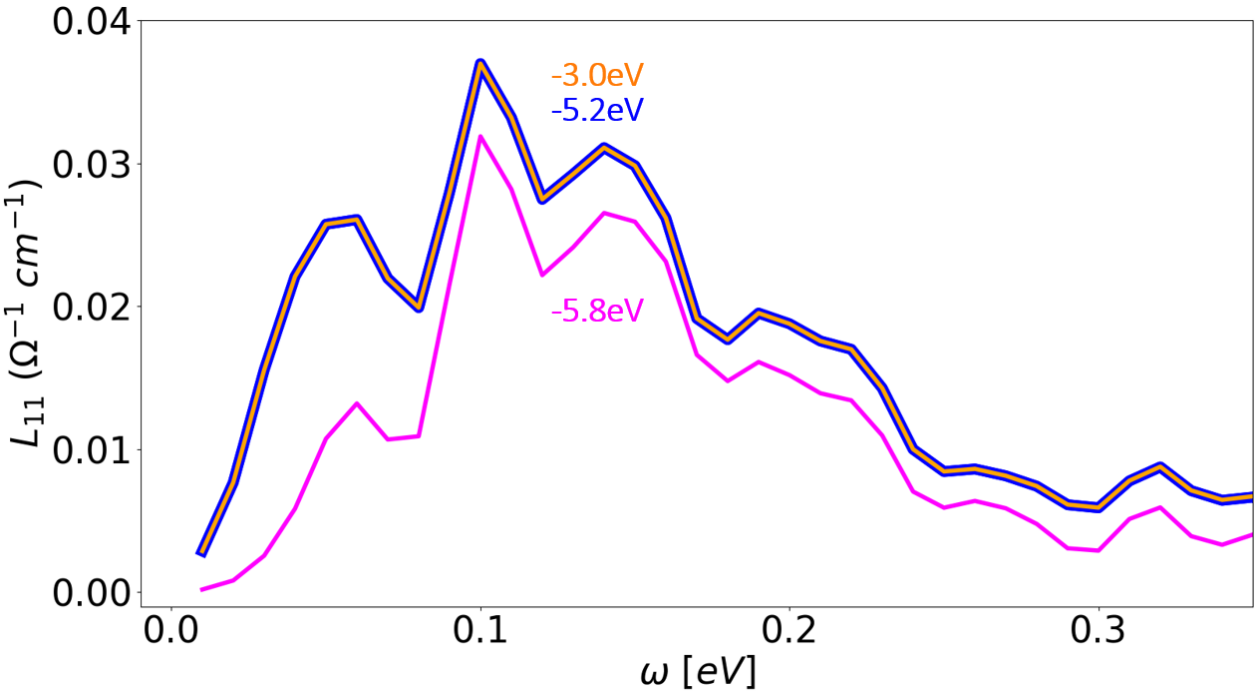


**Figure 3.4.:** Comparison of the $L_{11}$ spectrum of a single sample (64 Si atoms, 300K) for different upper boundaries of the energy window. The lower boundary was fixed at -6.2eV. The spectra for an upper boundary of -5.8eV and -5.2eV show significant differences, while the ones for -5.2eV and -3.0eV match so well, that their blue and orange lines lie on top of each other.

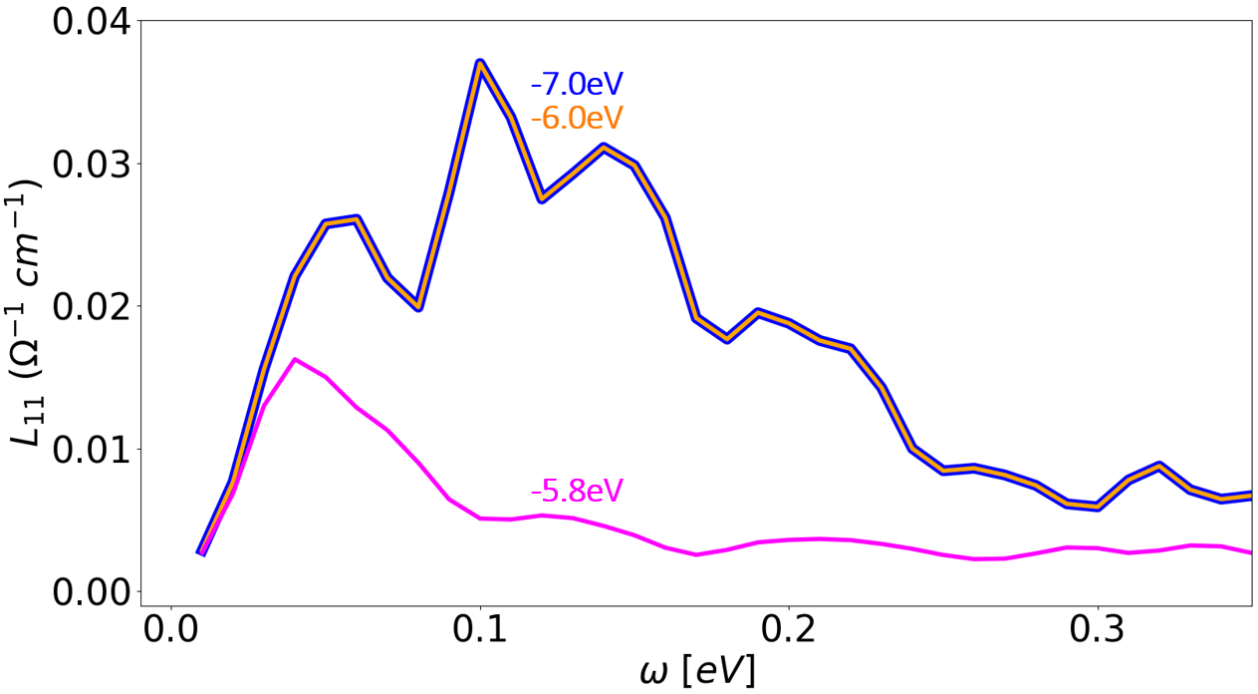


**Figure 3.5.:** Comparison of the $L_{11}$ spectrum of single sample of 64 Si atoms at 300K for different lower boundaries of the energy window. The upper boundary was fixed at -5.2eV. The spectra for a lower boundary of -5.8eV and -6.0eV show significant differences, while the ones for -6.0eV and -7.0eV match so well, that their blue and orange lines lie on top of each other.

## 3.4. The k-grid Convergence of a Single Sample

In this section, we investigate the behaviour of the $L_{11}$ spectrum for increasingly high **k**-grid densities. In the first subsection, we show results and costs of the original implementation without Fourier interpolation and in the second subsection with the application of Fourier interpolation.

### 3.4.1. Without Fourier Interpolation

The $L_{11}$ spectrum converges much slower than the total energy with respect to the **k**-grid density. At the 4x4x4 **k**-grid in the 64 Si-atoms supercell the total energy and the electronic density are already converged. However, the KG spectra are still underconverged at this **k**-grid density, as shown below. Therefore, the **k**-grid density must be increased, until the changes in the spectrum from one **k**-grid density to the next higher density become negligible. But higher **k**-grid densities come with higher computational costs, which must be controlled, too.

Starting at the 4x4x4 **k**-grid, for which the total energy is already converged, we calculated the $L_{11}$ spectrum for a randomly chosen, single sample with a 4x4x4, 8x8x8 and 16x16x16 **k**-grid.

We increased the **k**-grid density always by a factor of 2 in each direction to get commensurable **k**-grids, which ensure that the previous **k**-points remain in the denser **k**-grids. This assists the

comparability of the spectra. In total, the **k**-grid density is increased by a factor of 8 as the **k**-grid density is increased by a factor of 2 in each of the three spatial dimensions.

Significant differences between the $L_{11}$ spectra of the 4x4x4, 8x8x8 and 16x16x16 **k**-grid can be observed in figure 3.6. No quantitative convergence with respect to the **k**-grid is found.

Besides the $L_{11}$ spectrum, we also monitor the computation time and maximum memory per node. Let us emphasise that these calculations were performed with the original implementation, i.e., without Fourier interpolation. Accordingly, all **k**-points considered for KG, e.g. 16x16x16, are included in the SCF cylce, even if the much coarser 4x4x4 **k**-grid would suffice for total energy convergence.

The computational costs grow linearly with the number of **k**-points (figure 3.7). 48GB of maximum memory per node are allocated for the densest 16x16x16 **k**-grid. This leads to a maximum memory estimate of 384GB for the 32x32x32 **k**-grid, well beyond typical random-access memory (RAM) capacities on high-performce computing nodes. In principle, this issue can be solved by memory paralellization. However, there is a more advantageous route: Using Fourier interpolation, we can reduce computational costs, especially memory-wise, and investigate higher **k**-grid densities, as the next section shows.

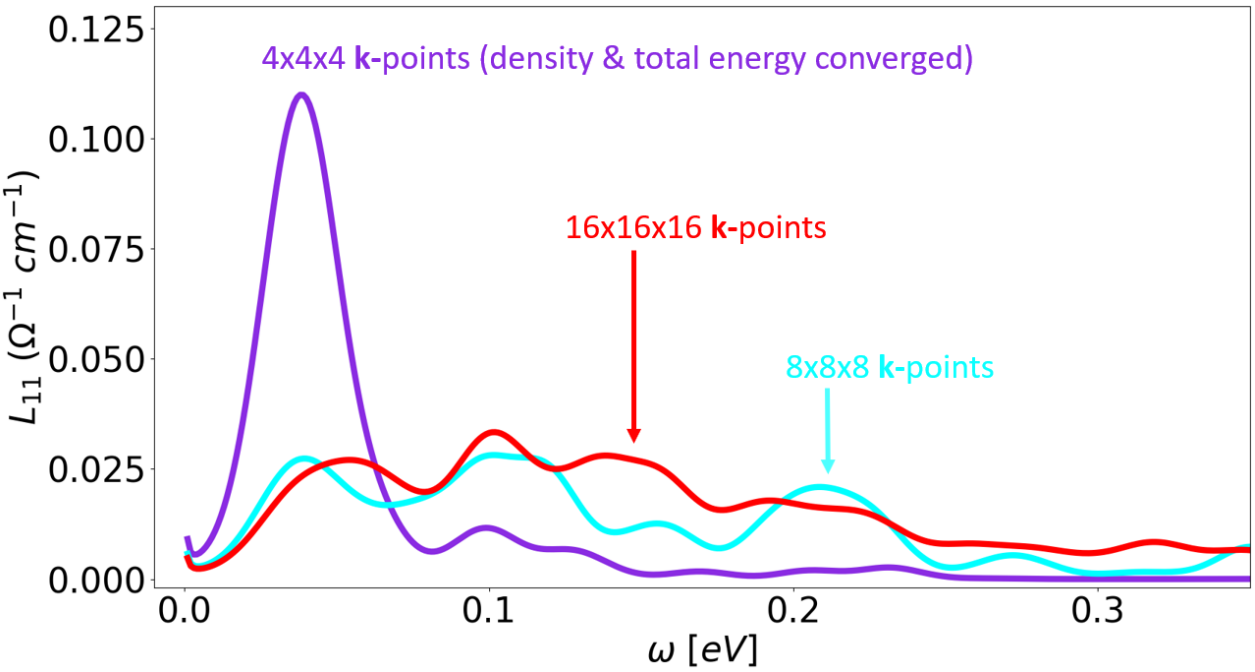


**Figure 3.6.:** Transport spectrum $L_{11}(\omega)$ for different **k**-grids. Starting from a 4x4x4 **k**-grid, for which the total energy is converged already, no quantitative convergence can be seen for the transport spectrum as we increase the number of **k**-points by a factor of 8 to 8x8x8 and another factor of 8 to 16x16x16.

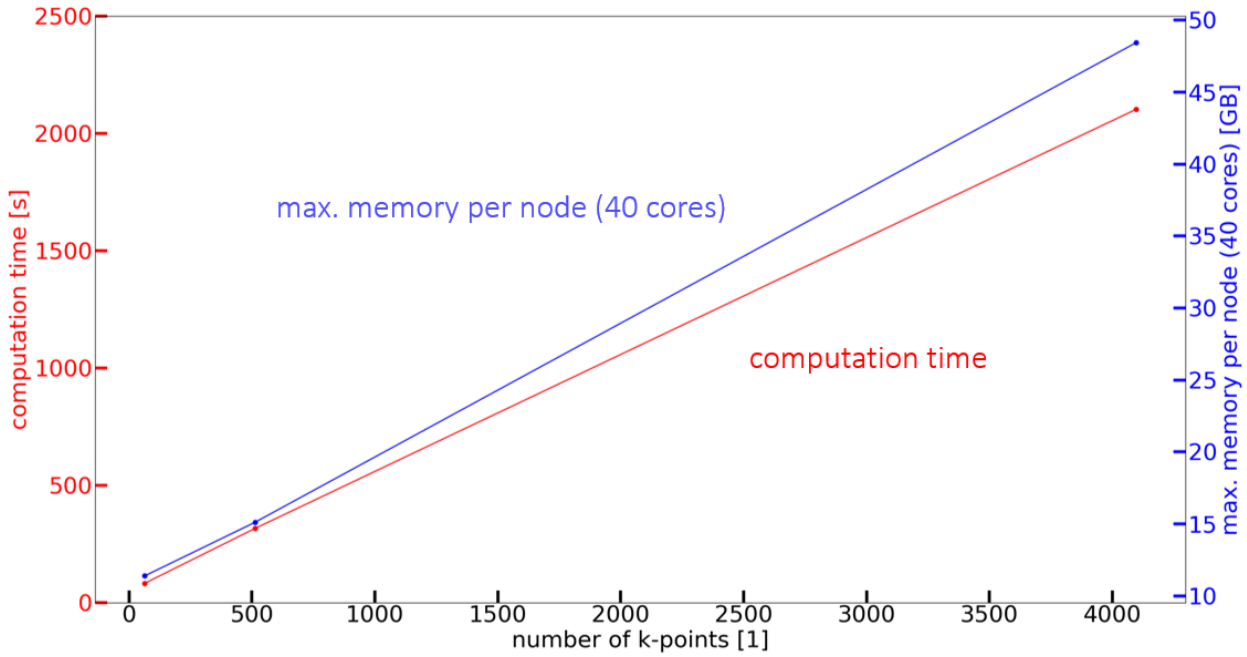


**Figure 3.7.:** Computation time and maximum memory per node grow linearly with the number of **k**-points. The computational costs for the underconverged **k**-grids are already considerable.

### 3.4.2. With Fourier Interpolation

With the Fourier interpolation we can converge the $L_{11}$ spectrum with respect to the **k**-grid, as we demonstrate in this section.

As we have seen in the former subsection 3.4.1, the $L_{11}$ spectrum of a supercell with 64 Si atoms is underconverged with respect to the **k**-grid at 16x16x16 and we are unable to make the next commensurable step to a **k**-grid of 32x32x32 at reasonable computational costs. Thus we need to cut computational costs in order to achieve **k**-grid convergence. To cut costs, we will use the Fourier interpolation to obtain denser **k**-grids from sparse **k**-grids. Because of the strictly localised nature of FHI aims basis set, this is not an approximation as long as the sparse **k**-grid is still dense enough to yield a converged Hamiltonian in real space, as shown in figure 3.8. In this way, we do not apply an approximation here, but take a more efficient way to the same result.

To demonstrate the agreement, we calculate a spectrum for the same 16x16x16 **k**-grid once without and once with Fourier interpolation. In figure 3.8, the spectrum without Fourier interpolation (red) and the spectrum with Fourier interpolation (black) are lying on top of each other. This manifests that the Fourier interpolation can exactly reproduce the electronic structure without Fourier interpolation, if the underlaying SCF **k**-grid is sufficiently dense.

Satisfied with the level of agreement provided by the Fourier interpolation, we increase the density of Fourier interpolated **k**-grid and calculate 32x32x32 and 64x64x64 to keep the **k**-grids commensurable as explained in the former subsection 3.4.1.

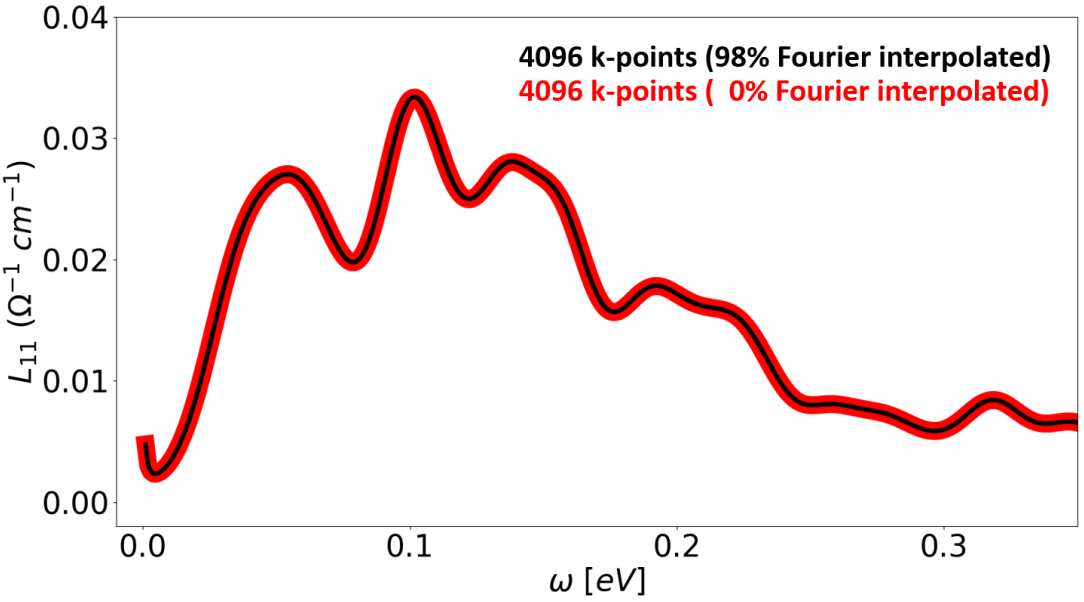


**Figure 3.8.:** Comparison of two transport spectra: one exclusively calculated with 16x16x16 SCF **k**-grid (red), the other, for which a 4x4x4 SCF **k**-grid has been extended by Fourier interpolation to a 16x16x16 **k**-grid (black). The SCF calculation and the Fourier-interpolated calculation show exact agreement even though 98% of the electronic states were calculated with the Fourier interpolation.

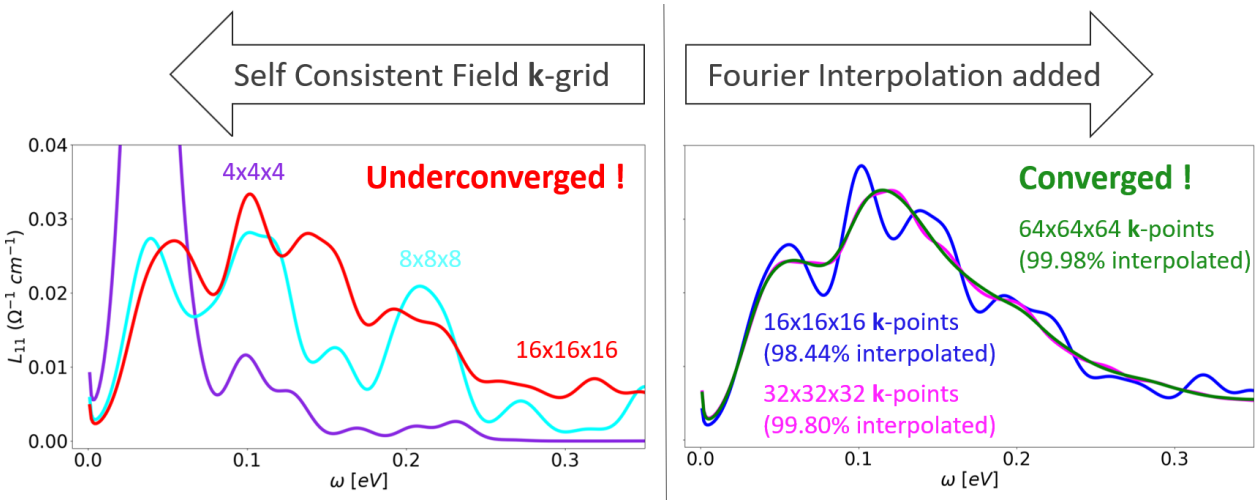


**Figure 3.9.:** Comparison of the transport spectra, which were exclusively calculated with SCF **k**-points on the left-hand side, with the transport spectra, for which a 4x4x4 SCF **k**-point grid has been extended by Fourier interpolation on the right-hand side. The red curves on the left-hand side and the blue curve on the right-hand side were calculated for the same number of **k**-points, but on the right-hand side, 98% of these **k**-points have been computed with the Fourier interpolation. On the right-hand side, the number of **k**-points can now be increased further due to the decreased cost. The two curves for the 32x32x32 and 64x64x64 **k**-grid on the right-hand side are hard to distinguish, which demonstrates the **k**-point convergence of the spectrum, that has now become feasible.

In contrast to the former situation, we can calculate the 32x32x32 and 64x64x64 **k**-grid successfully after cutting the costs by the Fourier interpolation.

The spectra of the 32x32x32 and 64x64x64 **k**-grid in figure 3.9 show a strong quantitative agreement. We have converged the single-sample $L_{11}$ spectrum of silicon with respect to the **k**-grid.

The application of the Fourier interpolation massively reduces the computational costs. After exploring the new regime of **k**-point densities that has become feasible by the application of the Fourier interpolation, let us compare quantitatively the computational cost of the transport spectra with 100% SCF **k**-grids and the **k**-grids extended by Fourier interpolation. For this, we look at the computation time and the maximum memory per node as in the former subsection in figure 3.10.

The computational time for the same amount of **k**-points can be cut in half by the application of the Fourier interpolation. Nevertheless the computational time continues to grow with the number of **k**-points under the application of Fourier interpolation.

The maximum memory per node, on the other hand, can be kept constant, because the Fourier interpolated **k**-points can be computed batch by batch after the SCF cycle in a postprocessing step. This casts into sharp relief the steep linear increase of memory costs, which is found with 100% SCF **k**-points (see figure 3.7).

This clearly illustrates the savings in computational cost. It shows that we could increase the **k**-grid density even further without running short of memory. Thus the application of the Fourier interpolation is an important step forward to overcome one of the key challenges in KG transport. We will continue to employ the Fourier interpolation for determining an appropriate choice of the broadening parameter and for the calculation of the thermodynamical average in the next sections.

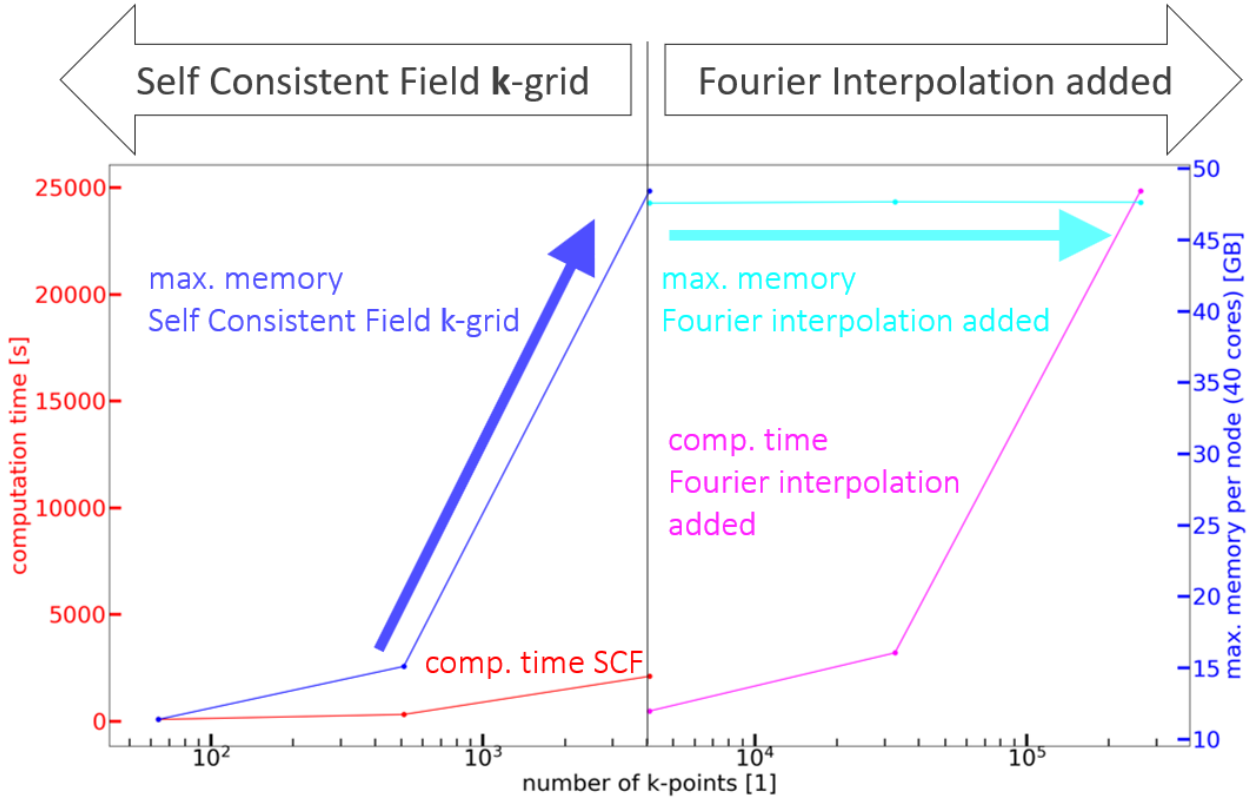


**Figure 3.10.:** Comparison of the computational costs for the 100% SCF **k**-grid (left), the **k**-grid extended with Fourier interpolated points (right). The left half was displayed before as figure 3.7, in which the linear increase of computational costs with the number of **k**-points was depicted. Here, the same relation has a nonlinear visualisation, because the horizontal axis has a logarithmic scale. The application of the Fourier interpolation massively reduces the computational costs: For the 16x16x16 **k**-grid the computational time is cut in half. The maximum memory per node can be kept constant, while extremely dense **k**-grids are computed.

## 3.5. The Broadening Parameter

Similar to the $\omega$-sampling rate, the broadening is a numerical parameter, which needs to be chosen carefully due to its strong influence on the resulting spectrum. Here, we present how we chose the broadening parameter in a systematic fashion.

In the Kubo-Greenwood formula (2.57), we replaced Dirac's $\delta$-function with Gaussian to make the formula numerically evaluable. Since the $\delta$-function is infinitesimally narrow, an adequate Gaussian replacement should be chosen as narrow as possible.

A narrower Gaussian width, however, requires denser **k**-grids for obtaining smooth $L_{11}$ spectra.

We now explain first, why we expect a smooth spectrum schematically and then show that more **k**-points are needed for the **k**-grid convergence of calculations with smaller broadening in the following subsection.

### 3.5.1. Interplay of Broadening and k-grid Convergence

To clarify the relationship between the Gaussian width and **k**-grid density, let us first consider a single **k**-point. Because of the continuity of the energy bands, the energy structure in the close neighbourhood of this **k**-point will have high similarity with the energy structure at the **k**-point itself. Thus the close neighbourhood of the chosen **k**-point will give a similar $L_{11}$ contribution at a similar $\omega$. This results in smooth $L_{11}$ spectra. Too low **k**-grid densities can lead to rough $L_{11}$ spectra, though.

To clarify this, let us assume a reduced system. Here only three $\omega$-points are sampled (see figures 3.11, 3.12, and, 3.13). Their corresponding transition energies (green bars) are translated to be searched for in the electronic band diagram. The band diagram is assumed to consist of only two straight bands, one flat and the other one with a constant slope (orange lines in figures 3.11, 3.12, and 3.13). To each of the sharp energies (green bars), a tolerance for matching transitions is added by the Gaussian broadening (first standard deviation in light green). The electronic structure is sampled at only two **k**-points (light purple corridors) in figure 3.11. To keep things simple, we assume that the same $L_{11}$ contribution (blue circles) to a certain $\omega$ is made, if a **k**-point samples the band diagram and shows a transition energy within the first standard-deviation tolerance of $\omega$ at this **k**-point (i.e. the upper orange band, light purple and light green corridors overlap).

The resulting $L_{11}$ spectrum shows intensities for the higher and lower frequency, but no intensity for the medium frequency (figure 3.11). However, the electronic structure contains a contribution to the medium frequency as well. It is just not sampled.

To transform this jagged spectrum in figure 3.11 into a smooth one, one has two options: Either to provide more **k**-points (figure 3.12) or to increase the broadening (figure 3.13).

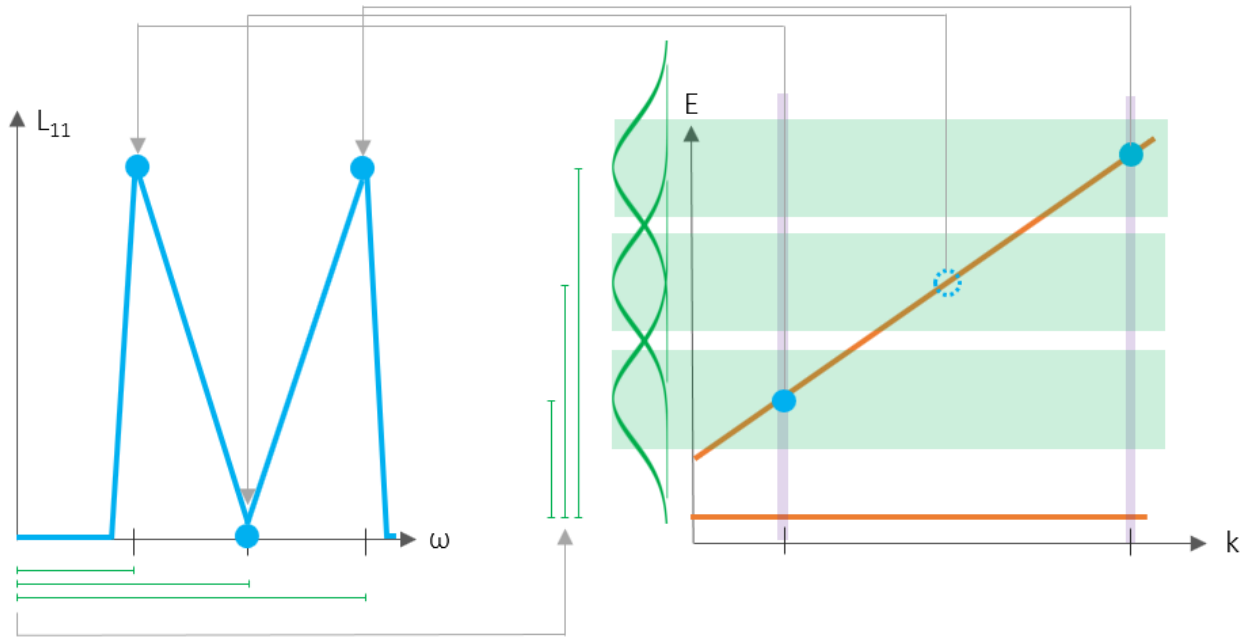


**Figure 3.11.:** Schematic explanation of the roughness in the spectrum, which arises from insufficient **k**-sampling, not from the electronic structure. The jagged $L_{11}$ spectrum is shown on the left, the corresponding electronic band structure on the right. The electronic bands (orange) are assumed to be straight for simplicity. The small corridors in light purple show sampled **k**-points. The light green background indicates the broadening, i.e., the first standard deviation of the Gaussian. We have consciously chosen the $\omega$-sampling and broadening such that is not covering the complete energy axis (white spaces between the corridors of the first standard deviation) for clarity's sake and in contrast to the advice we give in section 3.2. The zero intensity at the medium frequency stems from insufficient **k**-sampling (dashed blue circle).

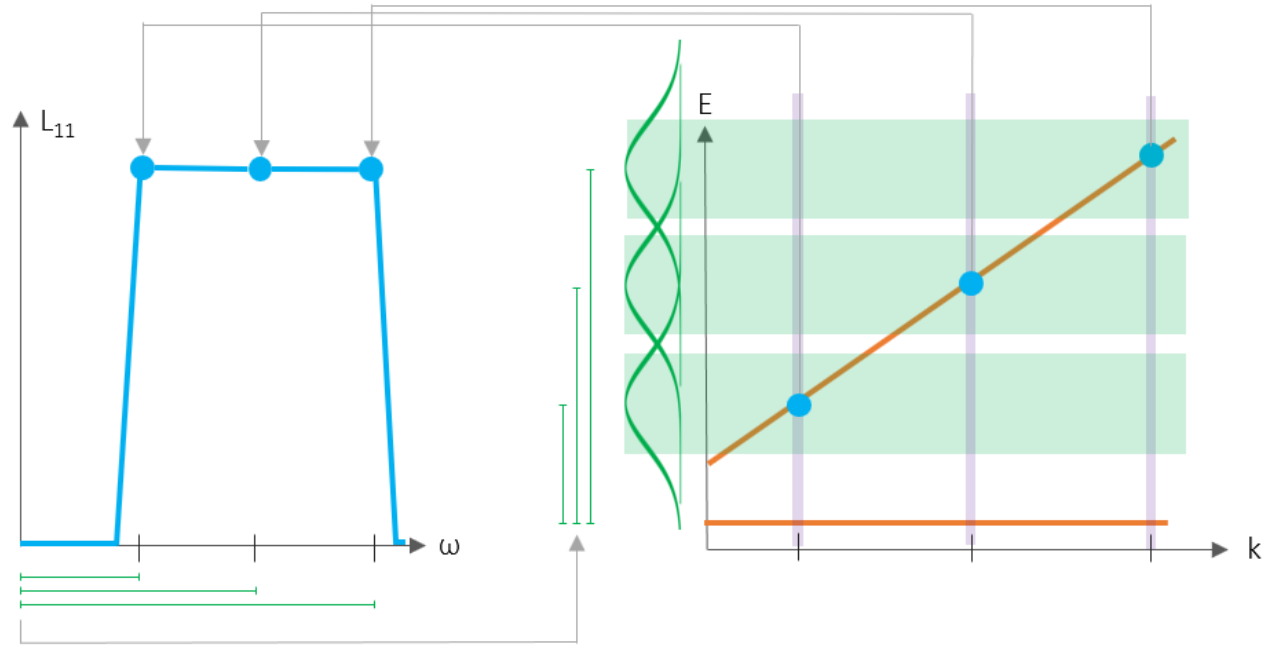


**Figure 3.12.:** Denser **k**-grid sampling removes the roughness in the $L_{11}$ spectrum shown in figure 3.11. Same entities and color coding as in figure 3.11.

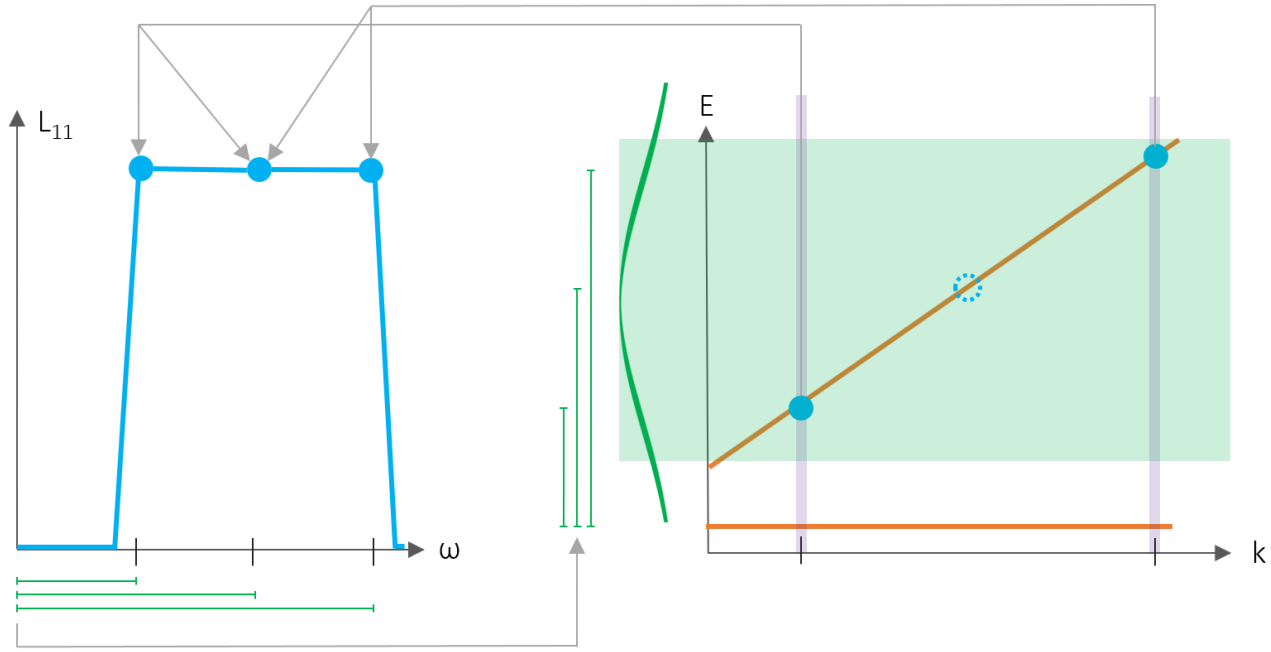


**Figure 3.13.:** Larger broadening, i.e., larger tolerance, removes the roughness in the $L_{11}$ spectrum shown in figure 3.11 by including transitions with energies, which are quite different from the energy originally searched for. Same entities and color coding as in figure 3.11. Only the Gaussian broadening for the medium frequency is shown here for clarity's sake, but of course the higher and lower frequency have the same large Gaussian broadening.

To obtain meaningful results, it is thus necessary to converge the **k**-grid for each broadening width independently. In a second step, one can then compare (**k**-grid converged) $L_{11}$ spectra with different widths to make an appropriate choice for the broadening parameter that balances accuracy and computational costs. Therefore we have investigated the **k**-grid convergence of the broadenings 1meV, 10meV, and, 100meV.

With a large broadening of 100meV, a very smooth curve with no resemblance to a Drude-like behaviour is seen (figure 3.14a), because the Drude peak is overshadowed by contributions on the left-hand and right-hand side of the spectrum, which extend far beyond their locations because of the large broadening. High intensities from the right-hand side stem from the beginning interband transitions and high intensities from the left-hand side from the factor $\frac{1}{\omega}$ in the Kubo-Greenwood formula (2.57), which diverges as $\omega$ approaches zero. The green and magenta line perfectly match each other. Thus the spectrum is converged with 4096 **k**-points for a 100meV broadening.

With a medium broadening of 10meV, the spectrum changes qualitatively when compared with the 100meV broadening: Towards small energies and small frequencies, the curve raises, peeking at a local maximum at ≈0.12eV, with a slight Drude-like behaviour [2] (figure 3.14b). The green and magenta line show very strong agreement. Thus the spectrum is converged with 32768 **k**-points for 10meV broadening, i.e., convergence is observed with eight times more **k**-points when compared to the large 100meV broadening.

With an even smaller broadening of 1meV, the curve is not smooth anymore, but jagged (figure 3.14c). The roughness however is reduced as the number of **k**-points grows. This behaviour is in line with our previous considerations, where we explained how the roughness of a spectrum decreases with larger broadenings or more **k**-points. In contrast to the former cases, we have not fully converged this spectrum with respect to the **k**-grid to not waste computational time, since we clearly see how the spectra tend towards a common average with increasing number of **k**-points.

2 The difference to the Drude curve should not be overrated, since a Drude curve is expected only in the average over a thermodynamical ensemble and here we are investigating only a single sample.

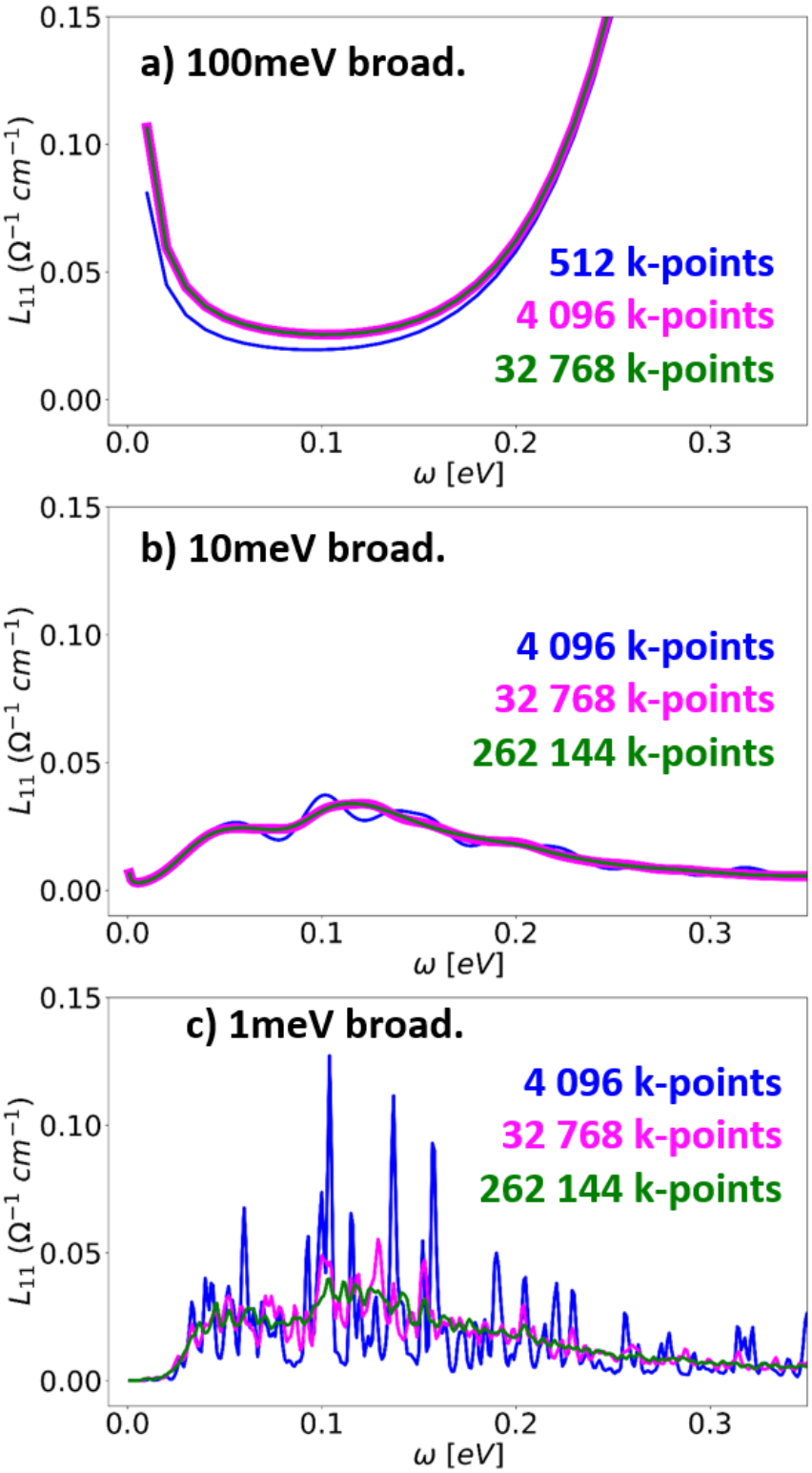


**Figure 3.14.:** The k-point convergence of $L_{11}$ spectra for different broadenings.

### 3.5.2. Convergence with the Broadening Parameter

We have now seen the two conflicting goals: minimal broadening and as few **k**-points as possible. The task at hand is to choose an optimal balance between these conflicting interests.

To do so, we look at the **k**-point converged curves of 1meV, 10meV, and 100meV broadening in one plot (figure 3.15). We see a qualitative agreement between the 1meV and the 10meV spectrum with only small quantitative differences, which will be even more neglectable in the thermodynamical average relevant for the final result (see section 3.6). The 100meV spectrum on the other hand strongly disagrees with the other ones. In consideration of figure 3.14, the 1meV curve shows a convergence towards the 10meV spectrum with increasing number of **k**-points. It is reasonable to assume that the oscillations of the 1meV spectrum would become even smaller, if more **k**-points were used. The 1meV and the 10meV spectrum show agreeing results, but the 10meV spectrum comes at a substantially lower computational price. Therefore we opt to continue with the 10meV broadening for the rest of this thesis.

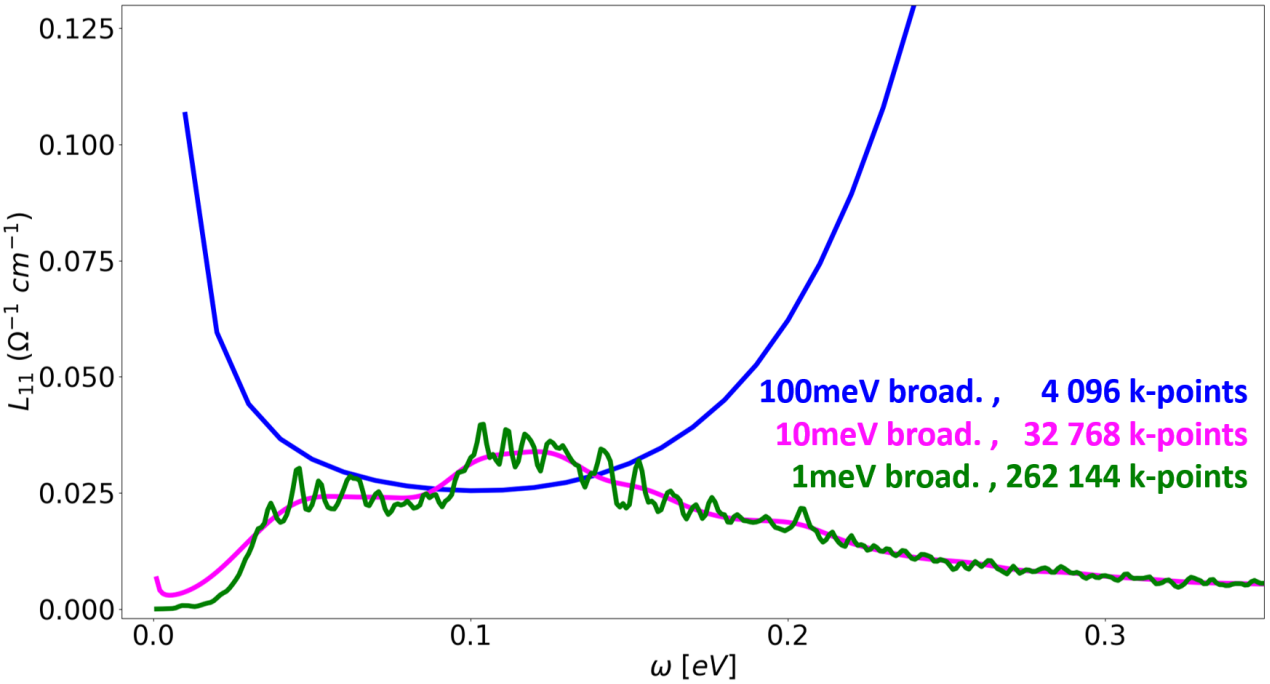


**Figure 3.15.:** The **k**-grid converged spectra from the former figure for all three broadenings. The 100meV broadening spectrum strongly disagrees with the spectra of smaller broadenings, but the spectrum for 1meV broadening oscillates around the 10meV broadening spectrum. Considering the higher costs and the thermodynamical average with its smoothing effect, the deviations between 1meV broadening and 10meV broadening are tolerable. Thus we opt to continue with the cheaper 10meV broadening.

In this section, we have seen how to choose the broadening parameter systematically: We start with a large broadening parameter and increase the number of **k**-points until converged. We then choose a significantly smaller broadening parameter and **k**-point converge this spectrum as well. If we find strong agreement between the spectra of different broadenings, we can assume that the

larger broadening provides a sufficient resolution. If the curves disagree, we reduce the broadening once more and proceed as before until the two spectra with the smallest, different broadenings sufficiently agree. One can then safely proceed with the larger one of the two smallest broadenings to further calculations.

The **k**-densities necessary to make this assessment have become accessible by the application of the Fourier interpolation. This systematic approach can easily be transferred to other materials and will provide certainty in the choice of the broadening parameter there as well.

## 3.6. DC-Mobility from the Ensemble Average

The DC-carrier mobility in silicon is determined with a thermodynamical ensemble average and a Drude extrapolation in this section.

Having studied the **k**-point convergence of the $L_{11}$ spectrum of a single sample, we now turn to the thermodynamical average over an ensemble of samples. As discussed in subsection 2.8.1, the Kubo-Greenwood formula must be averaged over a thermodynamical ensemble to provide the spectrum of electrical conductivity. We must thus create a thermodynamical ensemble, compute the single-sample spectra and average over them. The ensemble size must be sufficiently large. Therefore we have generated 90 samples with harmonic sampling and show the average $L_{11}$ spectra for ensembles of different sizes in figure 3.16: The average over 5 samples (red) and over 15 samples (orange) display clearly smaller values respectively larger values than the most representative average over 90 samples (blue) at their local maxima, while the average over 30 samples (green) is fluctuating around the 90-samples average with tolerable deviations.

The average over the 90 samples is now converted from the electrical conductivity $L_{11}(\omega)$ into the mobility $\mu(\omega)$ of carriers (electrons and holes together, blue curve in figure 3.17) for the following reason: The local density approximation (LDA) has been used to calculate the electronic structures. The LDA is notorious for a significant underestimation of the band gap [51]. A band gap, which is too small, would lead to carrier densities, which are too high. To circumvent this undesired effect, the electrical conductivity $L_{11}(\omega)$ is converted into the mobility $\mu(\omega)$ by dividing $L_{11}(\omega)$ by the free carrier density found at 300K in the electronic structure obtained for the nuclear geometry at 0K.

To extrapolate the DC mobility, we fit the Drude curve (red line in figure 3.17) to the average between the first local maximum and the first local minimum, which occurs before interband contributions become visible in the average mobility spectrum around 0.4eV (not displayed in this figure). That the ensemble size is chosen sufficiently large can be seen qualitatively by the smooth, Drude-like behaviour and quantitatively by the controlled error (blue area in figure 3.17), which was computed as the standard deviation between the averages of independent ensembles of 30 members each. As a comparison, we integrated the rougher spectrum of the randomly chosen, single sample into the plot, for which the former convergence tests have been performed.

Comparing with the Drude fit (red in figure 3.17) with the thermodynamic ensemble average (blue), the different behaviour towards small frequencies close to $\omega$=0.00eV is striking: The ensemble mobility (blue) is decreasing from its local maximum at $\omega$=0.08eV towards $\omega$=0.00eV, while the Drude

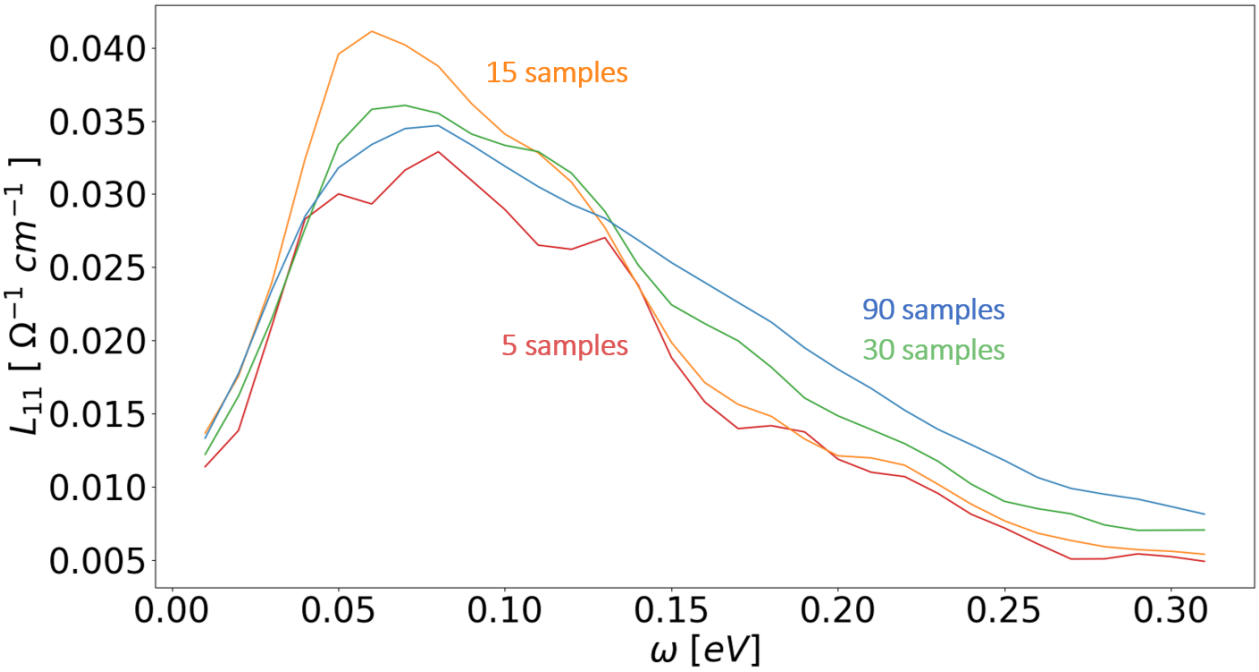


**Figure 3.16.:** The thermodynamical average over the $L_{11}$ spectra of ensembles of different sizes is shown. Around their local maximum the average over 5 samples (red) and 15 samples (orange) exhibit clearly smaller respectively larger values than the most representative average over 90 samples (blue). The 30-samples average (green), however, is fluctuating around the 90-samples average with tolerable differences. The KG calculation for the samples is performed with a 16x16x16 **k**-grid and a broadening of 10meV with all other computational parameters converged as determined in the previous sections for a single sample.

fit (red) is increasing towards $\omega$=0.00eV. The cause for this differing behaviour is the decreasing probability to sample electronic states with a vanishing energy difference at a certain **k**-point. An energy difference of zero at the same **k**-point is rarely sampled, since they can only be found where two bands cross each other. For larger supercells, however, this probability increases due to the folding of the band diagram and the Drude peak will approach the vertical axis allowing a more reliable extrapolation.

Because of the particular emphasis on **k**-grids in this work, we show a convergence study of the ensemble average with the **k**-grid in the next section 3.7.

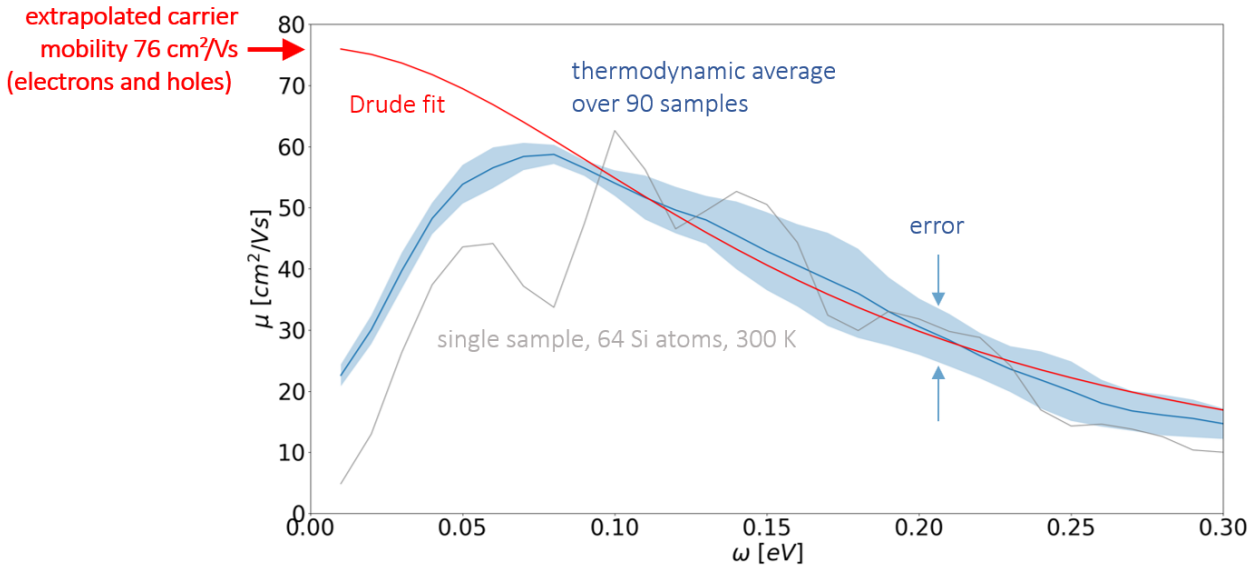


**Figure 3.17.:** The average over the mobility $\mu(\omega)$ of 90 samples (blue, 16x16x16 **k**-points, 98% interpolated) exhibits the smooth shape of a Drude curve, while an exemplary single sample (grey) shows considerable deviations from this smooth behaviour. The error is computed as the standard deviation of three independent ensembles with 30 samples each (light blue area). Fitting a Drude curve to the average, the extrapolated direct–current carrier mobility at $\omega = 0$eV reads 76cm$^2$/Vs.

## 3.7. The k-grid Convergence of the Ensemble Average

The final quantity, which we are interest in, is the DC conductivity of the ensemble average. Thus it is worth to investigate the **k**-grid convergence of DC conductivity of the ensemble average. Therefore we compute the extrapolated DC conductivity for the same ensemble with different **k**-grids.

We determine the DC mobility for each **k**-grid configuration in the same way as displayed in detail in the previous section 3.6. To investigate solely the influence of the **k**-grid on the extrapolated direct-current mobility, the exact same harmonic samples constitute the ensemble and only the **k**-grid density for the calculation of each sample is varied. The DC mobility for the 4x4x4 and 8x8x8 **k**-grid deviate from each other strongly by a factor of more than three, while the mobilities of 16x16x16 and 32x32x32 agree with each other within a tolerance of less than 3%. The runs 4x4x4 and 8x8x8 **k**-grid are clearly underconverged. Convergence of the ensemble average starts at the 16x16x16 **k**-grid.

Note that the single-sample convergence started at 32x32x32 (cf. figure 3.9), while the convergence of the extrapolated ensemble mobility starts earlier at 16x16x16. This suggests, that the single sample spectra are qualitatively converged at 16x16x16, but quantitative deviations upwards and downwards exist. In the ensemble average, these deviations cancel out and convergence can be observed at the 16x16x16 **k**-grid already. The next section provides a comparison with the experimental value.

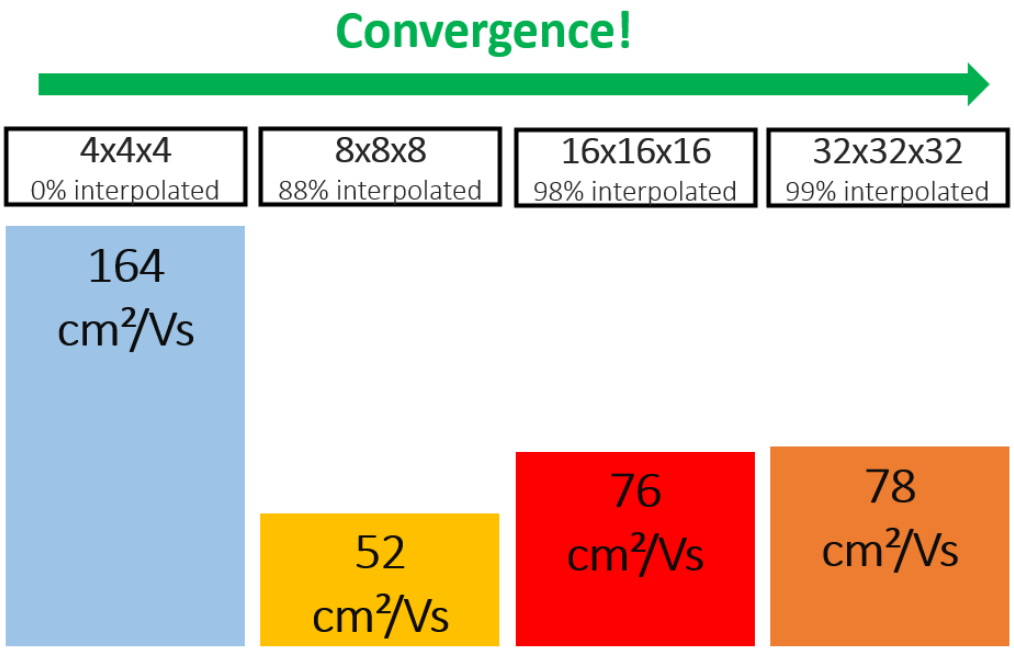


**Figure 3.18.:** Convergence of the extrapolated direct-current mobility of the ensemble average with increasing number of **k**-points.

## 3.8. Comparison with Experiment

In this section, we point out several potential sources of inaccuracies in the presented calculations and compare our result with the experimental reference value. Let us first discuss the sources of potential inaccuracies.

1) We have used the local density approximation of the exchange-correlation functional, which is not only known for its underestimation of band gap energy, but also shows deviations of the effective masses when compared to more accurate GW calculations [52]. This points out that the LDA captures the electronic structure of silicon with a certain error. While predicted conductivities would be severely wrong by orders of magnitude, due to the band gap errors, mobilities should only be affected by ±32% [16].

2) Using harmonic sampling instead of snapshots from a MD trajectory, we have assumed that silicon is a perfectly harmonic material, which is a valid approximation for silicon, but certainly not a perfect model. Still one expects this error to be much smaller than 10% [53].

3) Furthermore we have been working with a 64-atom supercell. This is the most sever source of error. The finite-size effect can be compensated for by an extrapolation to the infinite-supercell limit. For the infinite-supercell extrapolation, we plot the mobilities over $1/N$ with $N$ the number of atoms for the 64, 512 and 1024 atoms supercell, fit a straight line through these datapoints and read the mobility value at the intersection point of the vertical axis with the fitted straight line at $1/N = 0 \leftrightarrow N = \infty$. However, the result of the infinite-supercell extrapolation is preliminary, since we were not able to compute a sufficient number of samples with 512 or more atoms, yet, whose **k**-grids have the required convergence density. The challenge here is, that we want to compute the

512-atom supercell with an SCF **k**-grid of 2x2x2, but for this big supercell we would like to employ more than 8 supercomputer nodes. This means that a single **k**-point is calculated on more than one node. Thus a sophisticated parallelisation is needed. The supercell convergence is not topic of this thesis though. To implement this is challenging and now pursued by other members of the group.

After these considerations, we compare our calculated result with the experimental reference value [54]: Our computed result for the DC conductivity of Si approaches the experimental value with a preliminary extrapolation to the infinite supercell. Without the infinite-supercell extrapolation, our extrapolated result is more than one order of magnitude too small in comparison with the experimental value (see figure 3.19). For this deviation, an important factor is the insufficient sampling in phonon **q**-space, which results in an undersampling of the intraband contributions to the conductivity. Only direct transitions at the same **k**-points are taken into account by our implementation (see section 2.8.2). For a primitive unit cell, this means a complete neglection of intraband contributions. But by going to larger supercells and the subsequent folding of the band diagram due to the reciprocal relationship between real space and **k**-space, more **q**-points become accessible and one can map the intraband contributions onto interband contributions (see figure 3.20). The presented preliminary extrapolation points in this direction.

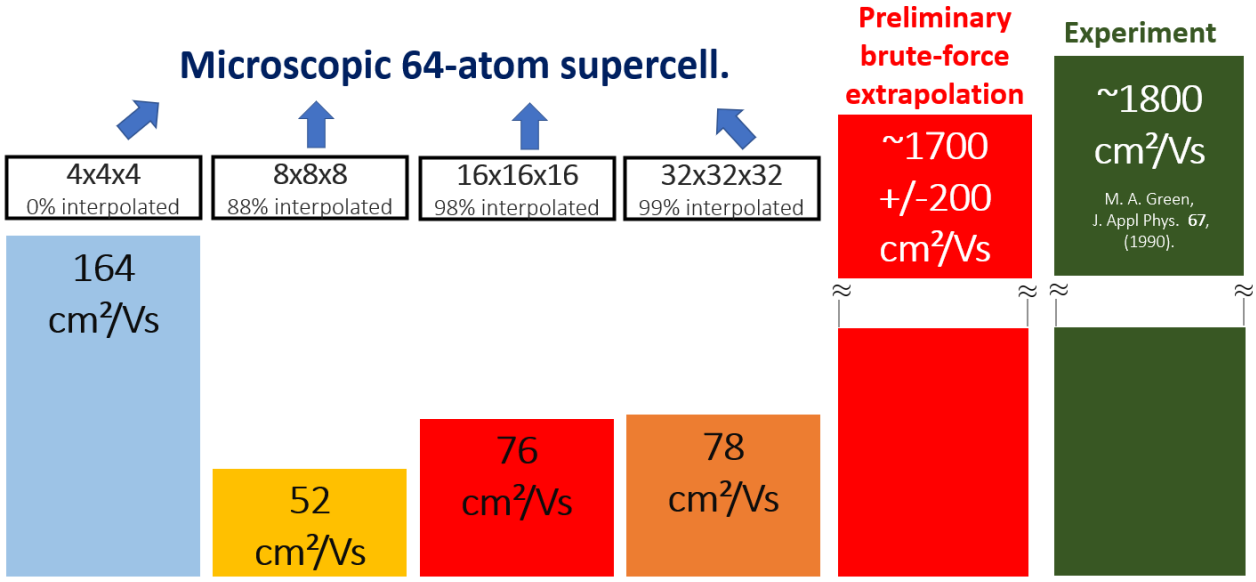


**Figure 3.19.:** In comparison with the experiment, the DC carrier mobility of the 64-atom supercell shows a difference of more than one order of magnitude. But if we extrapolate this result to the infinite-supercell limit, our result approaches the experimental value.

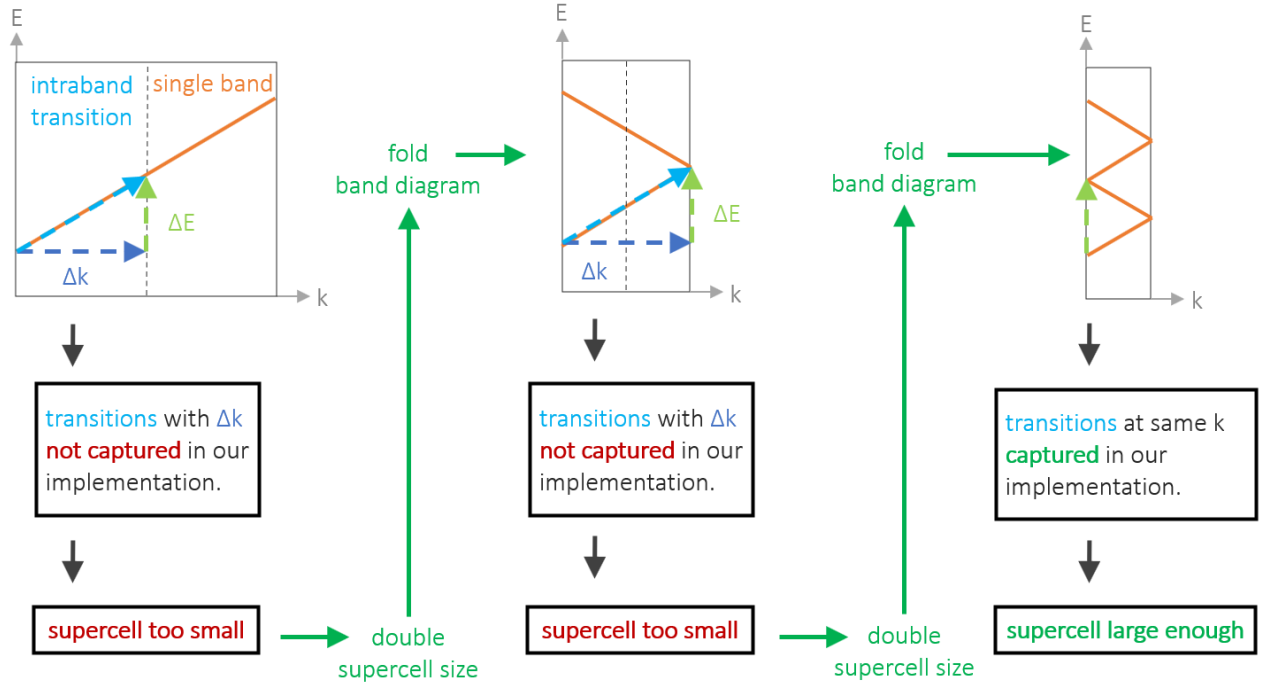


**Figure 3.20.:** The intraband contribution to conductivity is not captured in our implementation in band diagrams without folding. But by employing larger supercells and the subsequent folding, an intraband contribution can be mapped onto an interband contribution, which is taken into account.

# 4. Summary and Outlook

## 4.1. Summary

The Kubo-Greenwood approach is an appealing way to predict electronic transport properties in solid materials, which naturally include all orders of anharmonicity. However, its practical applicability is limited because of the immense computational costs, which are especially high for semiconductors due to the **k**-space localisation of the free carriers.

After the swift generation of an thermodynamical ensemble by harmonic sampling and converging the electrical-conductivity spectrum with respect to the other computational parameters, we have concretely shown this computational challenge of converging the electrical-conductivity spectrum with respect to the **k**-grid density for the prototypical semiconductor silicon. To make **k**-grid convergence feasible, we then applied the Fourier interpolation. Thereby we have been able to **k**-point converge the electrical-conductivity spectrum of single samples and the thermodynamical ensemble of this challenging material, because the Fourier interpolation opens up a new region of **k**-grid densities for Kubo-Greenwood calculations. This greatly alleviates one of the two key computational issues of the Kubo-Greenwood approach.

Even though the more efficient generation of **k**-points by Fourier interpolation assists the investigation of larger supercells, an additional challenge needs to be overcome: the supercell convergence. Our preliminary, brute-force extrapolation indicates encouraging results. However, more involved extrapolation procedures that do not require the explicit calculations of large supercells would be desirable. Fourier interpolation strategies that act on both, the electronic **k**- and the phononic **q**-space, seem like a natural solution to this problem. Their implementation, however, goes beyond the scope of this thesis.

## 4.2. Outlook

Further efficiency improvements may be realized with an inhomogeneously spaced **k**-grid, which is especially dense at those regions in the Brillouin zone, which matter most for the electronic transport. The most important regions are the **k**-spaces volumes containing electronic states closest to the Fermi level. In semiconductors these are namely the valence band maximum and the conduction band minimum.

To reap the benefits of the Fourier interpolation also at larger supercells, the code must be parallelised in such a way that the number of employed cores can exceed the number of **k**-points of the SCF **k**-grid, since in large supercells very sparse SCF **k**-grids are sufficient for the Hamiltonian to converge. Further **k**-points necessary for the convergence of the transport spectra can then be computed in the postprocessing with the Fourier interpolation.

The achieved **k**-point convergence of the transport spectrum of the challenging semiconductor silicon suggests that the same success is now feasible also for many other crystalline materials. By that, we are taking an import step towards a single, electronic transport prediction framework that can deal with all kinds of materials.

# Appendix

# A. The Search for more Efficient Thermoelectrics - an Opportunity for the Kubo-Greenwood Approach

A current research topic with tremendous technological potential is the efficient conversion of waste heat into electrical energy via the Seebeck effect. For an economic, large-scale application, the current thermoelectrical materials are too inefficient. To assist the search of more efficient thermoelectrics from the theoretical side, thermoelectrical transport predictions that include anharmonicities are desirable.

When generating electrical energy in a power plant, more thermal waste heat is produced than electrical energy (see figure A.1). Recovering even a fraction of the waste heat in power plants could save vast amounts of resources, but the application is not limited to power plants: In almost every technological process waste heat is accumulated, from industrial processes to computers over cars to washing machines.


**Figure A.1.:** More thermal waste heat than electrical energy has been produced by US power plants in 2012 fueled by coal, natural gas and nuclear [55]. Transforming even a fraction the thermal waste heat into electrical energy would be of great benefit.

Thermoelectrical materials can convert heat into electrical energy and are thus suitable for this task. However, their efficiency is still too small for an economic large-scale application. In consequence, many research teams are looking for more efficient thermoelectrics. The efficiency of a thermoelectrical material is characterised by its dimensionless figure of merit $zT$:

$$zT = \frac{\sigma S^2 T}{\kappa}\,, \tag{A.1}$$

where $T$ is the absolute temperature in Kelvin, $\sigma$ the electrical conductivity, $S$ the Seebeck-coefficient, and $\kappa$ the thermal conductivity [56]. As shown by this formula, an efficient conversion benefits from high electrical conductivity and low thermal conductivity (see figure A.2).

Materials with low thermal conductivity have an interesting property: They tend to have a high anharmonicity scores [57] (see Figure A.3). Thus efficient thermoelectrics are typically anharmonic materials.

The anharmonicity measure $\sigma^A$ of a material at temperature $T$ in figure A.3 is defined as:

$$\sigma^A(T) = \frac{\sigma[F^A]_T}{\sigma[F]_T} = \sqrt{\frac{\sum_{I,\alpha}\langle (F^A_{I,\alpha})^2\rangle_T}{\sum_{I,\alpha}\langle (F_{I,\alpha})^2\rangle_T}}\,, \tag{A.2}$$

where $F$ are the full forces, $F^A$ the anharmonic forces, $\langle\cdot\rangle_T$ the mean over a thermodynamical ensemble at temperature $T$, $I$ is the index of an atom, and $\alpha$ indicates the spatial direction.

To assist the search of more efficient thermoelectrics from the theoretical side, thermoelectrical transport predictions that include anharmonicities are therefore desirable. The Kubo-Greenwood approach provides such a prediction framework. However, it is associated with high computational costs. For some materials these computational costs are so high, that reliable predictions were practically infeasible. With this thesis, we overcome one of the two key computational hurdles and thereby pave the way towards affordable, fully anharmonic predictions of electronic heat and charge transport coefficients.

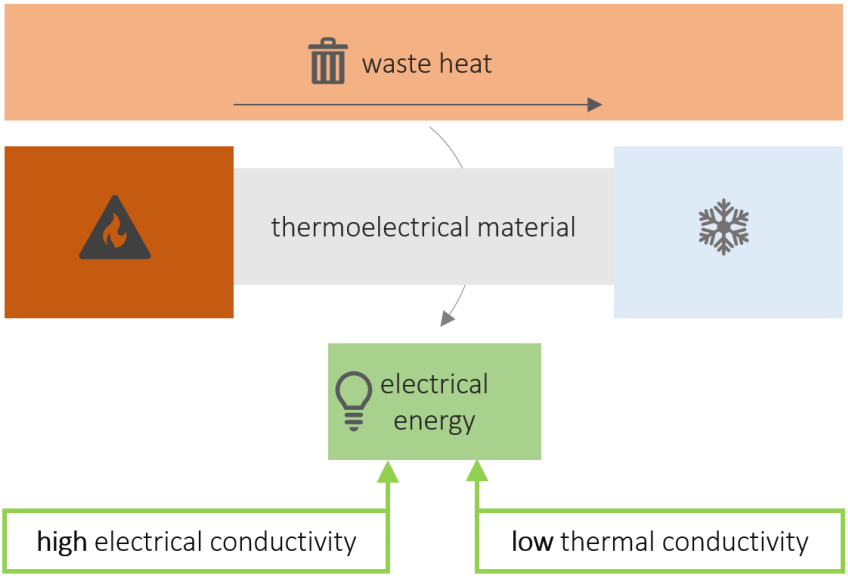


**Figure A.2.:** Thermoelectric material, connected to a hot reservoir on the left and a cool reservoir on the right, converts the temperature gradient partly into a gradient of the electrical potential, i.e. useful voltage. The conversion efficiency of a material benefits from high electrical and low thermal conductivity.

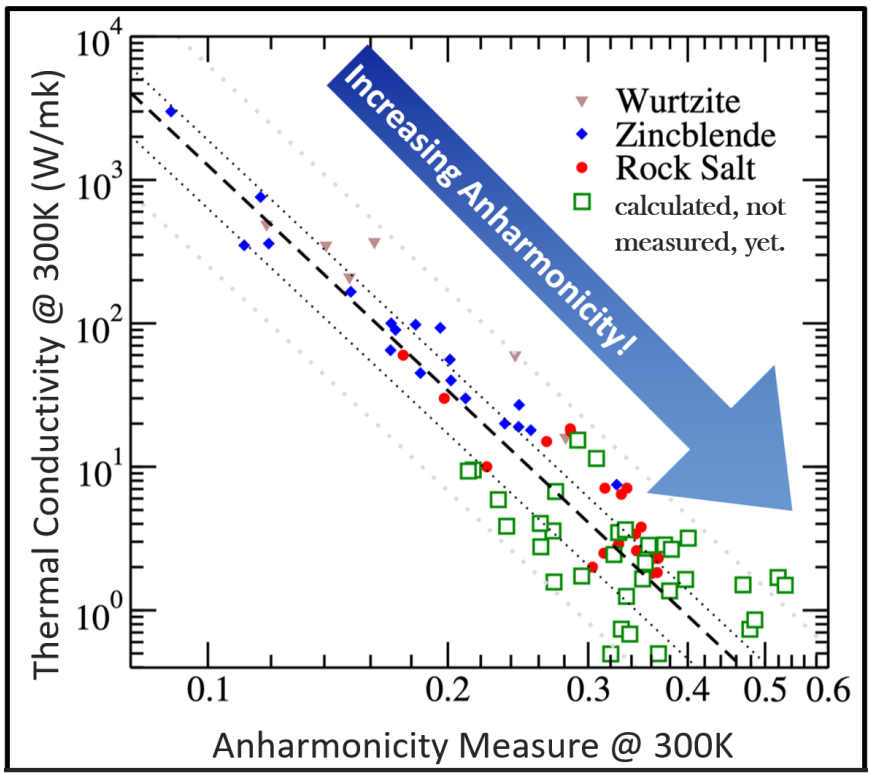


**Figure A.3.:** Low thermal conductivity and anharmonicity correlate. Low thermal conductors and with them efficient thermoelectrics can thus typically be found among materials with high anharmonicity. The green squares show materials, whose thermal conductivities were not experimentally measured, yet. Calculations of their anharmonicity measures however suggests that their thermal conductivities are expected to be low. Following calculations of their thermal conductivities corroborate this hypothesis. This exemplifies that the anharmonicity measure is a useful hint for thermal-conductivity predictions. Figure adapted from [58].

# Bibliography


[1] **M. Malki**, **C. M. Hoo**, **M. L. Mecartney and H. Schneider**: "Electrical Conductivity of Mullite Ceramics", Journal of the American Ceramic Society **97**, 1923–1930 (2014).

[2] **O. Madelung**, **editor**: *Semiconductors — Basic Data*, en (Springer, Berlin, Heidelberg, 1996).

[3] **National Institute of Standards and Technology (U.S.)**: *Circular of the Bureau of Standards No. 31 3rd Edition: Copper Wire Tables*, techreport (**october** 1914).

[4] **R. Franz and G. Wiedemann**: "Ueber die Wärme-Leitungsfähigkeit der Metalle", Annalen der Physik **165**, 497–531 (1853).

[5] **P. Drude**: "Zur Elektronentheorie der Metalle", Annalen der Physik **306**, 566–613 (1900).

[6] **P. Drude**: "Zur Elektronentheorie der Metalle; II. Teil. Galvanomagnetische und thermomagnetische Effecte", Annalen der Physik **308**, 369–402 (1900).

[7] **F. Bloch**: "Über die Quantenmechanik der Elektronen in Kristallgittern", Zeitschrift für Physik **52**, 555–600 (1929).

[8] **G. D. Mahan**: *Many-Particle Physics*, en (Springer US, Boston, MA, 2000).

[9] **R. Kubo**: "Statistical-Mechanical Theory of Irreversible Processes. I. General Theory and Simple Applications to Magnetic and Conduction Problems", Journal of the Physical Society of Japan **12**, 570–586 (1957).

[10] **R. Zwanzig**: "Time-Correlation Functions and Transport Coefficients in Statistical Mechanics", Annual Review of Physical Chemistry **16**, 67–102 (1965).

[11] **B. Holst**, **M. French and R. Redmer**: "Electronic transport coefficients from ab initio simulations and application to dense liquid hydrogen", Physical Review B **83**, 235120 (2011).

[12] **D. Alfè**, **M. Pozzo and M. P. Desjarlais**: "Lattice electrical resistivity of magnetic bcc iron from first-principles calculations", Physical Review B **85**, 024102 (2012).

[13] **M. French and T. R. Mattsson**: "Thermoelectric transport properties of molybdenum from ab initio simulations", Physical Review B **90**, 165113 (2014).

[14] **L. Calderin**, **V. V. Karasiev and S. B. Trickey**: "Kubo-Greenwood Electrical Conductivity Formulation and Implementation for Projector Augmented Wave Datasets", Computer Physics Communications **221**, 118–142 (2017).

[15] **C. Di Paola**, **F. Macheda**, **S. Laricchia**, **C. Weber and N. Bonini**: "First-principles study of electronic transport and structural properties of $C_{12}Sb_4S_{13}$ in its high-temperature phase", Physical Review Research **2**, 033055 (2020).

[16] **S. Poncé**, **E. R. Margine and F. Giustino**: "Towards predictive many-body calculations of phonon-limited carrier mobilities in semiconductors", Physical Review B **97**, 121201 (2018).

[17] **F. Giustino**: *Materials Modelling using Density Functional Theory: Properties and Predictions* (Oxford University Press, Oxford, New York, **may** 2014).

[18] **S. Kurth and J. P. Perdew**: "Role of the exchange–correlation energy: Nature's glue", International Journal of Quantum Chemistry **77**, 814–818 (2000).

[19] **V. Fock**: "Näherungsmethode zur Lösung des quantenmechanischen Mehrkörperproblems", Zeitschrift für Physik **61**, 126–148 (1930).

[20] **P. Hohenberg and W. Kohn**: "Inhomogeneous Electron Gas", Physical Review **136**, B864–B871 (1964).

[21] **W. Kohn and L. J. Sham**: "Self-Consistent Equations Including Exchange and Correlation Effects", Physical Review **140**, A1133–A1138 (1965).

[22] **M. Gell-Mann and K. A. Brueckner**: "Correlation Energy of an Electron Gas at High Density", Physical Review **106**, 364–368 (1957).

[23] **P. Nozières and D. Pines**: "Correlation Energy of a Free Electron Gas", Physical Review **111**, 442–454 (1958).

[24] **D. M. Ceperley and B. J. Alder**: "Ground State of the Electron Gas by a Stochastic Method", Physical Review Letters **45**, 566–569 (1980).

[25] **D. Pines**: *Elementary excitations in solids*, Lecture notes and supplements in physics (Benjamin, New York u.a., 1963).

[26] **M. C. Payne**, **M. P. Teter**, **D. C. Allan**, **T. A. Arias and J. D. Joannopoulos**: "Iterative minimization techniques for ab initio total-energy calculations: molecular dynamics and conjugate gradients", Reviews of Modern Physics **64**, 1045–1097 (1992).

[27] **J. Paier**, **R. Hirschl**, **M. Marsman and G. Kresse**: "The Perdew-Burke-Ernzerhof exchange-correlation functional applied to the G2-1 test set using a plane-wave basis set", The Journal of Chemical Physics **122**, 234102 (2005).

[28] **V. Blum**, **R. Gehrke**, **F. Hanke**, **P. Havu**, **V. Havu**, **X. Ren**, **K. Reuter and M. Scheffler**: "Ab initio molecular simulations with numeric atom-centered orbitals", Computer Physics Communications **180**, 2175–2196 (2009).

[29] **M. Born and T. von Kármán**: "Über Schwingungen in Raumgittern", Physikalische Zeitschrift **13** (1912).

[30] **H. Hellmann**: "Einführung in die Quantenchemie", **in***~Hans Hellmann: Einführung in die Quantenchemie: Mit biografischen Notizen von Hans Hellmann jr.* (Berlin, Heidelberg, 2015), **pages** 19–376.

[31] **R. P. Feynman**: "Forces in Molecules", Physical Review **56**, 340–343 (1939).

[32] **M. T. Dove**: *Introduction to Lattice Dynamics*, Cambridge Topics in Mineral Physics and Chemistry (Cambridge University Press, Cambridge, 1993).

[33] **A. Togo and I. Tanaka**: "First principles phonon calculations in materials science", Scripta Materialia **108**, 1–5 (2015).

[34] **F. Knoop**, **T. Purcell**, **M. Scheffler and C. Carbogno**: "FHI-vibes: Ab Initio Vibrational Simulations", Journal of Open Source Software **5**, 2671 (2020).

[35] **W. Demtröder**: *Experimentalphysik 3: Atome, Moleküle und Festkörper*, Deutsch, 5. Aufl. 2016 Edition (Springer Spektrum, **june** 2016).

[36] **N. Mermin and N. Ashcroft**: *Solid State Physics*, New ed (Brooks/Cole, New York, **january** 1976).

[37] **I. Henins**: "Precision Density Measurement of Silicon", Journal of Research of the National Bureau of Standards. Section A, Physics and Chemistry **68A**, 529–533 (1964).

[38] **E. Schrödinger**: "Quantisierung als Eigenwertproblem", Annalen der Physik **385**, 437–490 (1926).

[39] **J. Smoliner**: *Grundlagen der Halbleiterphysik* (Springer, Berlin, Heidelberg, 2018).

[40] **P. A. M. Dirac and N. H. D. Bohr**: "The quantum theory of the emission and absorption of radiation", Proceedings of the Royal Society of London. Series A, Containing Papers of a Mathematical and Physical Character **114**, 243–265 (1927).

[41] **F. Giustino**: "Electron-phonon interactions from first principles", Reviews of Modern Physics **89**, 015003 (2017).

[42] **M. Fiorentini and N. Bonini**: "Thermoelectric coefficients of n-doped silicon from first principles via the solution of the Boltzmann transport equation", Physical Review B **94**, 085204 (2016).

[43] **F. Macheda and N. Bonini**: "Magnetotransport phenomena in p -doped diamond from first principles", Physical Review B **98**, 201201 (2018).

[44] **F. Caruso**, **M. Troppenz**, **S. Rigamonti and C. Draxl**: "Thermally enhanced Fröhlich coupling in SnSe", Physical Review B **99**, 081104 (2019).

[45] **J. B. Johnson**: "Thermal Agitation of Electricity in Conductors", Physical Review **32**, 97–109 (1928).

[46] **Z. Yuan**: "Electrical conductivity from frist principles", PhD thesis (Humbolth-Universität zu Berlin, Berlin, 2022).

[47] **P. D. Desai**: "Thermodynamic Properties of Iron and Silicon", Journal of Physical and Chemical Reference Data **15**, 967–983 (1986).

[48] **H.-H. Kowalski**: "Theory of Thermal Conductivity", PhD thesis (Technische Universität Berlin, Berlin, 2022).

[49] **A. M. Alvertis and E. A. Engel**: "Importance of vibrational anharmonicity for electron-phonon coupling in molecular crystals", Physical Review B **105**, L180301 (2022).

[50] **M. Ceriotti**, **G. Bussi and M. Parrinello**: "Nuclear Quantum Effects in Solids Using a Colored-Noise Thermostat", Physical Review Letters **103**, 030603 (2009).

[51] **J. P. Perdew and M. Levy**: "Physical Content of the Exact Kohn-Sham Orbital Energies: Band Gaps and Derivative Discontinuities", Physical Review Letters **51**, 1884–1887 (1983).

[52] **M. Bouhassoune and A. Schindlmayr**: "Ab Initio Study of Strain Effects on the Quasiparticle Bands and Effective Masses in Silicon", Advances in Condensed Matter Physics **2015**, 1–8 (2015).

[53] **M. Zacharias**, **M. Scheffler and C. Carbogno**: "Fully anharmonic nonperturbative theory of vibronically renormalized electronic band structures", Physical Review B **102**, 045126 (2020).

[54] **M. A. Green**: "Intrinsic concentration, effective densities of states, and effective mass in silicon", Journal of Applied Physics **67**, 2944–2954 (1990).

[55] **D. B. Gingerich and M. S. Mauter**: "Quantity, Quality, and Availability of Waste Heat from United States Thermal Power Generation", Environmental Science & Technology **49**, 8297–8306 (2015).

[56] **G. J. Snyder and E. S. Toberer**: "Complex thermoelectric materials", Nature Materials **7**, 105–114 (2008).

[57] **F. Knoop**, **T. A. R. Purcell**, **M. Scheffler and C. Carbogno**: "Anharmonicity measure for materials", Physical Review Materials **4**, 083809 (2020).

[58] **F. Knoop**, **T. A. R. Purcell**, **M. Scheffler and C. Carbogno**: "Anharmonicity in Thermal Insulators: An Analysis from First Principles", Physical Review Letters **130**, 236301 (2023).

# Danksagung

Ganz herzlich danke ich meinem Betreuer, Dr. Christian Carbogno, für seine sehr engagierte und überaus kompetente Begleitung durch das gesamte letzte Jahr hindurch. Durch seine Expertise und seine genauen Hinweise konnte ich inhaltlich und methodisch sehr viel dazulernen.

Prof. Dr. Matthias Scheffler möchte ich für das Ermöglichen der Teilnahme an zahlreichen Veranstaltungen zum wissenschaftlichen Austausch und dem Zugang zu Hochleistungsrechnern danken, sowie Prof. Dr. Andreas Knorr für seine sofortige Bereitschaft als Gutachter zu fungieren.

Allen Mitgliedern der Novel Material Discovery Group danke ich für fruchtbare Gespräche, insbesondere Jingkai Quan, der diese Arbeit weiterführt.

Dankbar bin ich außerdem meiner Freundin und meinen Eltern für ihre Unterstützung.